J. Fluid Mech. (2013), *vol.* 722, *pp.* 5–50. © Cambridge University Press 2013
doi:10.1017/jfm.2013.88

Growth and dissipation of wind-forced, deep-water waves

Laurent Grare[1,‡,†], William L. Peirson[2], Hubert Branger[1], James W. Walker[2,§], Jean-Paul Giovanangeli[1] and Vladimir Makin[3]

[1]Institut de Recherche sur les Phénomènes Hors Equilibre, CNRS UMR 6594, Aix-Marseille Université, France

[2]Water Research Laboratory, School of Civil and Environmental Engineering, University of New South Wales, King Street, Manly Vale NSW 2093, Australia

[3]KNMI, PO Box 201, 3730 AE De Bilt, The Netherlands

(Received 17 June 2011; revised 16 January 2013; accepted 9 February 2013; first published online 28 March 2013)

The input of energy by wind to water waves is compared with the observed growth of the waves using a suite of microphysical measurement techniques in the laboratory. These include measured tangential stresses in the water and air immediately adjacent to the interface with corresponding form drag measurements above wind-forced freely propagating waves. The drag data sets are consistent but the comparison has highlighted important issues in relation to the measurement of fluctuating pressures above freely propagating waves. Derived normalized wind input values show good collapse as a function of mean wave steepness and are significantly in excess of the assembly of net wave growth measurements by Peirson & Garcia (*J. Fluid Mech.*, vol. 608, 2008, pp. 243–274) at low steepness. Sheltering coefficients in the form of Jeffreys (*Proc. R. Soc. Lond. Ser.* A, vol. 107, 1925, pp. 189–206) are derived that are consistent with values previously obtained by Donelan & Pierson (*J. Geophys. Res.*, vol. 92, 1987, pp. 4971–5029), Donelan (*Wind-over-Wave Couplings: Perspectives and Prospects*, Clarendon, 1999, pp. 183–194) and Donelan *et al.* (*J. Phys. Oceanogr.*, vol. 36, 2006, pp. 1672–1689). The sheltering coefficients exhibit substantial scatter. By carefully measuring the associated growth of the surface wave fields, systematic energy budgets for the interaction between wind and waves are obtained. For non-breaking waves, there is a significant and systematic misclose in the radiative transfer equation if wave–turbulence interactions are not included. Significantly higher levels of turbulent wave attenuation are found in comparison with the theoretical estimates by Teixeira & Belcher (*J. Fluid Mech.*, vol. 458, 2002, pp. 229–267) and Ardhuin & Jenkins (*J. Phys. Oceanogr.*, vol. 36, 2006, pp. 551–557). Suitable normalizations of attenuation for wind-forced wave fields exhibit consistent behaviour in the presence and absence of wave breaking. Closure of the surface energy flux budget is obtained by comparing the normalized energy loss rates due to breaking with the values previously determined by Banner & Peirson (*J. Fluid Mech.*, vol. 585, 2007, pp. 93–115) and Drazen *et al.*(*J. Fluid Mech.*, vol. 611, 2008, pp. 307–332) when expressed as a function of mean wave steepness. Their normalized energy loss

† Email address for correspondence: lgrare@ucsd.edu

‡ Present address: UCSD, Scripps Institution of Oceanography, La Jolla, San Diego, CA 92093, USA.

§ Present address: Sogreah Gulf – Artelia Group, PO Box 18271, Dubai, UAE.

rates obtained for non-wind forced breaking wave groups are remarkably consistent with the levels found during this present study when breaking waves are subject to wind forcing.

Key words: surface gravity waves, wave breaking, wind–wave interactions

1. Introduction

Although energy budgets lie at the heart of many air–sea interaction phenomena, a fundamental quantitative understanding of the exchange of energy between wind, waves, dissipation and surface currents has remained elusive (Sullivan & McWilliams 2010, p. 23). The development of wave fields is understood in terms of a differencing of wind input and losses due to breaking with the balance mediated by nonlinear transfers between waves of different frequency or wavenumber (Phillips 1985). Distinguishing the precise relative significance of the input, loss and transfer components is complicated because of their (presumed) similarities in magnitude (Phillips 1985).

This absence of a fundamental understanding has not prevented the development of sophisticated representations of numerical sea states (e.g. Janssen 2004; Tolman 2009), near-surface current structure (Craig & Banner 1994; Mellor & Blumberg 2004) and elementary models of air–sea constituent exchanges (Wanninkhof *et al.* 2009). In spite of the essential coupling amongst wave field development, surface ocean currents and constituent exchanges, there has been little progress in reconciling different approaches because of ongoing fundamental knowledge gaps relating to the coupling of winds and waves.

Peirson & Garcia (2008) recently assembled a suite of laboratory measurements of net wave growth under the action of wind and found a systematic collapse of the data as a function of wave steepness: behaviour not predicted by conventional linear theories. Further, they found that the longstanding differences between measured and theoretically (or numerically) predicted growth may potentially be reconciled in terms of wave coherent tangential stresses, most importantly at low wave steepnesses. They also observed that there were few direct measurements of wind-energy input and any existing measurements have remained unreconciled with observations of net wave growth since the pioneering studies by Shemdin & Hsu (1967) and Bole & Hsu (1969).

The purpose of this present contribution is to report detailed studies to measure levels of wind-energy input to freely propagating wave fields, consequent growth in the laboratory with estimates of wave dissipation rates. Specifically, a series of experiments were conducted using a new mobile profiling instrument platform to measure tangential stress and form drag at the sea surface in a large wind–wave tank. The tangential stress was obtained from a novel kingfisher diving device (Grare 2009) using hot-wire anemometer technology. Complementary form drag measurements were obtained from the same platform operating as an interfacial wave follower fitted with a static pressure probe. The tangential stress measurements obtained using this new technique are reconciled against the measurements by Walker (2009) (see Peirson, Walker & Banner 2012).

In the remainder of this section, we review present theoretical understanding and a summary of the results of previous measurement campaigns. This is followed

by a description of the experimental facilities and methods used during the present investigation. The study results are then presented and discussed followed by a concise summary of the principal study conclusions and recommendations. A large appendix at the end of this article contains a derivation of the momentum flux equations written in the frame of a wave follower.

1.1. *Spectral decomposition*

Using similar notation to Komen *et al.* (1994, § I.2.5, p. 25*ff*), the local total mean energy density $\langle E \rangle$ of a spectrum of surface gravity waves propagating past a point can be evaluated as

$$\langle E \rangle = \rho_w g \left\langle \eta^2 \right\rangle = \rho_w g \iint E(\omega, \theta)\, \mathrm{d}\omega\, \mathrm{d}\theta \tag{1.1}$$

where ρ_w is the density of water, g is gravitational acceleration, E is the spectral energy density as a function of wave direction θ and wave angular frequency $\omega = 2\pi f$ and

$$E(\omega, \theta) = \tfrac{1}{2} a(\omega, \theta)^2 \tag{1.2}$$

where a is the linear wave amplitude.

The development of the wave field is determined by microphysical energy fluxes mediated by corresponding momentum fluxes which must be carefully partitioned to determine the relative contributions of the waves and the currents (Peirson & Garcia 2008, p. 246*ff*)

Wu, Hsu & Street (1977, 1979) reported spectral decomposition within very small frequency bands but previous analysis (Peirson & Belcher 2005) could not reconcile their findings with other studies. This present investigation shows that microphysical measurement accuracies are only capable of quantifying input to a band of waves in the vicinity of the spectral peak.

The development of the wave field is usually described by the wave energy balance equation (Komen *et al.* 1994, pages 33 and 47) which is modified to recognize the spatial gradients in wave properties to yield

$$\left.\frac{\mathrm{d}E}{\mathrm{d}t}\right|_{\Delta\omega} = S|_{\Delta\omega} \tag{1.3}$$

where S are wave field energy fluxes and wave properties will be assumed to apply at a mean angular frequency ω_p within a spectral band of width $\Delta\omega$. Wave properties in this study will be ascribed to this angular frequency.

The wave field energy fluxes are conventionally recognized to be as follows:

$$S = S_{in} + S_{nl} + S_{diss} \tag{1.4}$$

where S_{in} is energy input by the wind, S_{nl} are transfer of energy due to nonlinear wave–wave interactions and S_{diss} (a negative quantity) is the loss of energy from the wave field.

A variety of nonlinear interactions associated with the development of wind waves are recognized in the literature (Phillips 1977, §§ 2.8, 3.8, 3.9 and 4.4; Rapp & Melville 1990, figure 1). Many of these interactions are yet to be quantified by physical experiments in the laboratory or the field. For experiments undertaken with wave frequency imposed by an initiating mechanical wave generator, the primary nonlinear interactions are the development of Benjamin & Feir (1967) instabilities which are readily observed and monitored within the measured wave spectra. For

developing fields of pure wind waves, the situation is more complicated due to the spectral downshifts which can be observed with fetch. Our approach here is to capture the dominant nonlinear interaction fluxes within a fixed bandwidth. This approach was vindicated by subsequent analysis of the gathered data. The spatial rate of change of the total energy density at frequencies above and below the selected bandwidth were found to be less than 1 % of those within the fixed bandwidth. Therefore, the S_{nl} flux from the selected bandwidth to lower frequencies was negligible in comparison with any other components within the bandwidth selected for analysis. The remaining two terms on the right-hand side (RHS) of (1.4) are now discussed in detail.

1.2. *Wind input*

1.2.1. *Theory*

The action of wind induces both momentum and energy fluxes to open water surfaces. The total momentum flux or the wind stress τ is the sum of the tangential stress (τ_{tang}) and the form drag (τ_{form}):

$$\tau = \tau_{tang} + \tau_{form} = \left\langle \tau_{visc} / \sqrt{1 + (\partial\eta/\partial x)^2} \right\rangle + \left\langle p_s \frac{\partial \eta}{\partial x} \right\rangle \tag{1.5}$$

where τ_{visc} is the local interfacial viscous surface tangential shear stress and p_s is the pressure at the interface, $\partial\eta/\partial x$ is the local interface slope and the angle brackets denote temporal or spatial averaging.

There is wind-induced energy flux to both the waves and the surface currents. Assuming linear spectral decomposition of the wave field, the source term in (1.5) becomes

$$S_{in} = \langle \tau_{visc} u_{s.wc} \rangle + \left\langle p_s \frac{\partial \eta}{\partial x} \right\rangle c \tag{1.6}$$

where $u_{s.wc}$ is the surface velocity coherent with frequency component ω, $\partial\eta/\partial x = ak \sin(kx - \omega t)$ and $c = g/\omega$ is the wave speed. When normalized by wave speed, the first term of (1.6) is termed the wave–coherent tangential stress τ_{wc} (see Longuet-Higgins 1969) and (1.6) becomes

$$S_{in} = \left(\tau_{wc} + \tau_{form}\right) c = \tau_{wave} c. \tag{1.7}$$

Consequently, the momentum flux leading to wave growth τ_{wave} has two components, the entire form drag and the wave coherent tangential stress.

There are two conventional characterizations of wind input that have been developed from theoretical considerations. The more widely appreciated is due to Miles (1957) and takes the form

$$\frac{S_{in}}{\omega E} = \beta \frac{\rho_a}{\rho_w} \left(\frac{u_*^a}{c} \right)^2 \tag{1.8}$$

where S_{in} is the energy input from the wind, β is a normalized growth coefficient, ρ_a is the density of air and $u_*^a = \sqrt{\tau/\rho_a}$ is the friction velocity.

The second was developed by Jeffreys (1925)

$$S_{in} = \frac{1}{2} \rho_a s_z (ak)^2 c^3 \left| \frac{U_z}{c} - 1 \right| \left(\frac{U_z}{c} - 1 \right) \tag{1.9}$$

where U_z and s_z are the wind speed and sheltering coefficient referenced at an elevation z above the mean surface, conventionally $z = \pi/k = \lambda/2$, where k is the wavenumber and λ is the wavelength.

1.2.2. *Measurement*

Equation (1.7) encapsulates the key quantities required to evaluate the wind-energy input to the waves. Measuring the wave–coherent tangential stress is an intricate process involving both surface shear and surface current. Given a prevailing belief that tangential stresses at the air–sea interface are small, fundamental research has primarily focused on developing reliable methods of measuring the surface pressures and correlating these with the surface slope.

A pioneering development was undertaken by Shemdin & Hsu (1967) who used a disc-shaped pressure sensor and transducer mounted on a moving platform which remained approximately 6 mm above the oscillating wave surface. They found good agreement with the theoretical predictions of wind input obtained by Miles (1959). Bole & Hsu (1969) found subsequently that the observed wave growth under the same conditions was an average of three times larger than the Miles (1959) values. That the net wave growth could be larger than the wind input in the absence of nonlinear transfers is implausible yet no direct comparisons incorporating direct appropriate measurements have been made to date.

A detailed field study reported by Snyder *et al.* (1981) completed an investigation incorporating near-surface pressure sensors in both fixed and wave-following modes. For wave ages $\left(c/u_*^a \sim 10\right)$, they found values of $\beta \sim 32$ (Plant 1982) but highlighted the strong influence of the spectral tail $\left(c/u_*^a < 0.3\right)$ in determining the wave-supported stress which they were unable to resolve. To the best of the authors' knowledge, their recommendation of further field investigation of the spectral tail has never been pursued.

Wu *et al.* (1977, 1979) completed further investigations in the same facility as Shemdin & Hsu (1967) with spectral decomposition of the input rates. These were found to be comparable with the original measurements of Shemdin & Hsu (1967).

Donelan (1999) used a surface-following pressure probe traversing waves generated with a JONSWAP spectral distribution by a paddle in a laboratory tank. Experiments were undertaken with the wind aligned and opposed to the direction of wave propagation. Donelan determined Jeffreys sheltering coefficients of $s_{\lambda/2}$ of 0.28 and 0.11 for the aligned and opposed directions, respectively.

Donelan *et al.* (2006) completed a field experiment in a lake using a wave follower in both fixed and following modes and achieved proximity to the surface of 2.1 cm. They concluded that air flow separation was an important feature of the wind input source function, reviewed a number of input parameterizations and concluded that a value of $s_{\lambda/2}$ of 0.17 best characterized their data.

In this present contribution, pressure–slope measurements are undertaken with the objective of reconciling them against corresponding measurements of the tangential stress.

Microscopic particle image velocimetry (PIV) using 20 μm particles and 7 μm image resolution was developed by Peirson (1997) for capturing the tangential stress and surface velocity at a moving air–water interface. This approach was applied by Banner & Peirson (1998) to quantify tangential stresses under a range of wind wave conditions. They concluded that the tangential stress remains a significant proportion of the total stress at moderate wind speeds but the wave–coherent tangential stress remained small. Further work by Peirson & Banner (2003) quantified the intensities of

vorticity associated with a range of surface features and explored the implications for low-solubility gas exchange. Recently, Peirson *et al.* (2012) at 4 μm image resolution re-applied the Peirson (1997) technique to developed waves, finding significant levels of tangential stress but very small wave–coherent stresses.

PIV techniques were developed using 10 μm water particles and 70 μm image resolution were applied on the air side of the interface by Veron, Saxena & Misra (2007). They found similar surface tangential stress distributions (their figure 2) to those captured by Banner & Peirson (1998, figure 5) and a strong relationship between surface velocity and the tangential stress. Wave–coherent tangential stresses were not presented.

1.3. *Losses from the wave field*

Four potential terms are recognized as contributing to S_{diss} as follows:

$$S_{diss} = S_{bed} + S_{visc} + S_{attn} = S_{bed} + S_{visc} + S_{break} + S_{turb}. \tag{1.10}$$

The term S_{bed} is the loss due to bottom friction. In deep water, negligible interactions with the bed occur, and S_{bed} is zero.

The term S_{visc} represents losses due to viscous effects near the free surface. These were carefully reviewed by Peirson *et al.* (2013), who found reasonable agreement with the following expression for waves of low steepness, assuming linear decomposition of the wave field:

$$S_{visc} = -2\mu_w a^2 k^2 g - \sqrt{2\rho_a \mu_a \omega} a^2 k g - \frac{2a^2 k g c_g}{b_t}\left(\frac{\rho_w \mu_w}{2\omega}\right)^{1/2} \tag{1.11}$$

where ρ_a and μ_a are the density and the dynamic viscosity of the air, ρ_w and μ_w are the density and the dynamic viscosity of the water, $(a,\ k, \omega, c_g)$ are the amplitude, the wavenumber, the pulsation and the group velocity of the dominant waves, respectively, and b_t is the tank width. The terms on the RHS of (1.11) are wave attenuation due to viscosity in, respectively, the surface aqueous layer, the surface air-side layer and the tank walls.

However, they observed a systematic increase of approximately 44 % in viscous loss for non-breaking waves with an increase in wave steepness from 0.1 to 0.15. In the absence of reliable parameterizations that incorporate steepness effects, in this study equation (1.11) is assumed to hold. This approach will be critically reviewed in the results and discussion section.

As recently discussed by Peirson *et al.* (2013), there has been a divergence in approaches to the surface non-viscous energy losses (Duncan 1983; Drazen, Melville & Lenain 2008; Tian, Perlin & Choi 2010) and so we preserve the quantity S_{attn} in (1.10) to represent these. Two potential contributions are conventionally recognized: S_{break}, representing energy losses due to surface breaking; and S_{turb}, energy losses due to Reynolds stress interactions between waves and subsurface turbulence. (We note in passing, that Ardhuin, Chapron & Collard (2009) have recently identified and quantified wave–turbulent interactions in the air for open ocean swell but these are insignificant in the context of the present study.)

The term S_{break} characterizes energy losses associated with breaking. The most widely used expression was developed by Phillips (1985) from the scaling argument of the energy dissipation introduced by Duncan (1981):

$$\frac{S_{break}(c)}{\Lambda(c)} = \varepsilon_L = \frac{b\rho_w c^5}{g} \tag{1.12}$$

where ε_L is the breaking energy loss rate per unit length of the breaking fronts and $\Lambda(c)$ is the length per unit area of breaking fronts moving at speed c. The coefficient b is a measure of breaking strength. Although it has been assumed that c_{break} is equivalent to c of the underlying wave form, there is a growing body of evidence (Rapp & Melville 1990; Banner & Peirson 2007) that c_{break} is less than c. Small differences can be significant in view of the large exponent in (1.12).

The quantity S_{turb} is the loss due to Reynolds stress interactions between waves and subsurface turbulence. This term is more controversial. Many investigators have assumed that $S_{turb} = 0$. Cheung & Street (1988) observed strong interactions between waves and near surface aqueous turbulence. Belcher, Harris & Street (1994) and Teixeira & Belcher (2002) have suggested that there is a significant reduction in wave growth rates arising from interactions between waves and turbulence: perhaps equivalent to 30 % of the total wind-energy input. Ardhuin & Jenkins (2006) critically reviewed the findings of Teixeira and Belcher and concluded that the interaction was much weaker, recommending a value approximate 20 % of the Teixeira and Belcher value. Peirson *et al.* (2013) have recently investigated wave attenuation by rainfall and found very strong wave attenuation when normalized by the subsurface turbulence while acknowledging the strong disruption of the interface by the rain itself.

2. Experimental facilities and methods

2.1. *Laboratory tanks*

2.1.1. *Large air–sea interaction facility at IRPHE*

One set of the experiments were conducted in the large wind–wave tank at the Institut de Recherche sur les Phénomènes Hors Équilibre (IRPHE) at Marseille. The tank's overall working section is 40 m long. It is 3.2 m wide with an air cavity 1.6 m high. Water depth was kept at 1 m. The tank is equipped with a controlled recirculating wind tunnel which can generate wind speeds between 2 and 14 m s^{-1}. A computer-controlled wave-maker can generate regular or random waves in a frequency range from 0.9 to 2.2 Hz. It is entirely submerged under the upstream beach to avoid any perturbation of the air flow which could be induced by its displacement.

The test section was placed at a fetch of 28 m. The upwind end of the tank is specially profiled to ensure minimum disturbance to either the generation of mechanical waves or the turbulent boundary layer in the airflow above the waves. The tunnel roof is carefully profiled to create an airflow boundary layer of zero pressure gradient along the test section. At the downwind end of the tank a permeable absorbing beach was installed to minimize wave reflection. A complete description of the tank can be found in Coantic *et al.* (1981).

In order to control the fetch in selected tests, a floating plastic sheet was positioned on the water surface, fastened at the upwind end of the tank. The floating plastic sheet remains flat when wind blows over it. Plastic sheet has often been used in the past to change the effective tank fetch while avoiding wind wave formation (Reul *et al.* 1999; Peirson, Garcia & Pells 2003; Plant *et al.* 2004).

The complete set of test conditions and the following key values are summarized in table 1: the fetch (column A), the wind speed at mid-depth of the air section U_m (column B), the frequency of applied monochromatic waves f_m (column C) and the observed peak spectral wave frequency f_p (column D). Also contained in table 1 are two measurements (runs 35 and BA) obtained by Mastenbroek *et al.* (1996) previously captured in the same IRPHE laboratory large tank, which have been retained in this study to provide a historical comparison with the present measurements. For these two

		A Fetch (m)	B U_m (m s^{-1})	C f_m (Hz)	D f_p (Hz)	E p_b (%)	F $c_{intrinsic}$ (m s^{-1})	G u_{drift} (m s^{-1})	H ak	I τ (Pa)	J z_0^a (m)	K $U_{\lambda/2}$ (m s^{-1})	L U_{10} (m s^{-1})	M τ_{tang} (Pa)
							Mastenbroek *et al.* (1996)							
	35	28.00	6.3	1.4	1.40	0	1.12	0.00	0.180	0.088	7.00×10^{-5}	5.7	7.8	0.018
	BA	28.00	5.4	1.4	1.40	0	1.12	0.00	0.150	0.057	3.69×10^{-5}	4.9	6.6	0.026
							Grare (2009)							
Large IRPHE facility	U7X315	3.15	7.0	0.0	7.70	100	0.30	0.09	0.110	0.064	7.80×10^{-5}	3.4	6.8	0.031
	U7X615	6.15	7.0	0.0	5.14	79	0.40	0.12	0.173	0.065	8.25×10^{-5}	3.7	6.8	0.025
	U7X915	9.15	7.0	0.0	3.94	53	0.49	0.12	0.195	0.078	1.61×10^{-4}	3.9	7.0	0.029
	U7X1215	12.15	7.0	0.0	3.36	42	0.56	0.12	0.196	0.085	2.55×10^{-4}	4.0	7.0	0.026
	U7X1515	15.15	7.0	0.0	2.93	38	0.62	0.11	0.194	0.088	3.97×10^{-4}	3.9	6.8	0.025
	U7X1815	18.15	7.0	0.0	2.66	32	0.68	0.10	0.192	0.090	4.08×10^{-4}	4.0	6.9	0.027
	U7X2265	22.65	7.0	0.0	2.33	26	0.75	0.09	0.183	0.092	4.31×10^{-4}	4.2	7.0	0.026
	U4F0	28.00	4.0	0.0	2.66	8	0.63	0.05	0.118	0.020	1.84×10^{-5}	2.9	4.3	0.009
	U5F0	28.00	5.0	0.0	2.29	10	0.73	0.04	0.144	0.033	1.84×10^{-5}	3.8	5.5	0.014
	U6F0	28.00	6.0	0.0	2.07	21	0.80	0.05	0.143	0.052	3.52×10^{-5}	4.5	6.5	0.026
	U7F0	28.00	7.0	0.0	1.95	25	0.86	0.07	0.160	0.081	4.64×10^{-5}	5.6	8.0	0.026
	U8F0	28.00	8.0	0.0	1.83	34	0.91	0.06	0.168	0.117	7.60×10^{-5}	6.4	9.2	0.035
	U9F0	28.00	9.0	0.0	1.71	40	0.97	0.07	0.199	0.168	1.27×10^{-4}	7.3	10.5	0.036
	U4F10	28.00	4.0	1.0	1.00	0	1.56	0.00	0.125	0.020	5.89×10^{-6}	3.8	4.6	0.008
	U4F12	28.00	4.0	1.2	1.20	0	1.30	0.00	0.178	0.024	1.37×10^{-5}	3.8	4.8	0.009
	U4F14	28.00	4.0	1.4	1.40	13	1.12	0.00	0.204	0.028	3.01×10^{-5}	3.6	4.9	0.008
	U7F10	28.00	7.0	1.0	1.00	0	1.56	0.00	0.100	0.073	1.61×10^{-5}	6.7	8.2	0.021
	U7F12	28.00	7.0	1.2	1.20	0	1.30	0.00	0.212	0.106	4.97×10^{-5}	6.9	9.1	0.023
	U7F14	28.00	7.0	1.4	1.40	43	1.12	0.00	0.256	0.147	1.93×10^{-4}	6.8	9.5	0.024
	U10F10	28.00	10.0	1.0	1.00	0	1.56	0.00	0.191	0.271	8.44×10^{-5}	10.9	13.9	0.037

TABLE 1. (Continued on next page)

		A Fetch (m)	B U_m (m s^{-1})	C f_m (Hz)	D f_p (Hz)	E p_b (%)	F $c_{intrinsic}$ (m s^{-1})	G u_{drift} (m s^{-1})	H ak	I τ (Pa)	J z_0^a (m)	K $U_{\lambda/2}$ (m s^{-1})	L U_{10} (m s^{-1})	M τ_{tang} (Pa)
							Peirson *et al.* (2012)							
Small WRL facility	F34U21AK27	2.40	2.1	3.4	3.40	0	0.46	0.00	0.270	0.059	1.40×10^{-4}	3.4	6.1	0.014
	F34U57AK32	2.40	5.7	3.4	3.40	100	0.46	0.00	0.320	0.331	3.30×10^{-4}	6.9	13.4	0.037
	F24U39AK24	2.40	3.9	2.4	2.40	0	0.65	0.00	0.240	0.125	1.64×10^{-4}	5.4	8.8	0.045
	F31U39AK28	2.40	3.9	3.1	3.10	100	0.50	0.00	0.280	0.216	1.03×10^{-3}	4.6	9.6	0.046

TABLE 1. Summary of experiment conditions. Present tangential stress measurements using the kingfisher and present form drag measurements using Elliott pressure disc (Grare 2009) were performed in the large IRPHE facility. Present measurements of the tangential stress using PIV techniques (Peirson *et al.* 2012) were performed in the small WRL facility. For previous measurements undertaken in the large IRPHE facility by Mastenbroek *et al.* (1996), the tangential stress values were derived from form drag measurements using (1.5).

runs, values of the form drag were computed by extrapolation of the measured out-of-phase pressure component and the tangential stress was derived from the difference between the total stress and the form drag. Present measurements undertaken in the large IRPHE facility are labelled, in table 1 and in the captions of the figures, as Grare (2009).

2.1.2. *Small wind–wave tank at the Water Research Laboratory*

The wind–wave tank used for the smaller-scale experiments of this study is linear, with an overall length of 8.95 m, width of 0.245 m and a total cavity height of 0.610 m. An electromechanical flexible cantilever paddle was used to generate monochromatic waves when necessary. Wind was generated by a fan fitted to one end of the tank. Guide vanes downwind of the fan ensured a uniform air flow across the width of the tank and provided a smooth transition from the inlet to the water surface. The tank is housed within a constant temperature room and was maintained at a temperature of $21.5 \pm 0.5\,^{\circ}\mathrm{C}$ throughout the presently reported experiments.

During all tests the total water depth was maintained at 247 ± 1 mm. The roof of the wind–wave tank is provided to achieve a zero pressure gradient along the length of the test section. A dissipative beach was installed at the downwind end of the fetch length to minimize wave reflections. All observations were taken at a fetch of 2.4 m. Measurements undertaken in the small Water Research Laboratory (WRL) facility are labelled, in table 1 and the captions of the figures, as Peirson *et al.* (2012).

2.2. *Wave measurement*

In both test facilities, conventional capacitance wave probes were used to capture the wave characteristics at high temporal resolution (200 Hz to capture a significant portion of the high-frequency tail). In each case, the probes were equipped with fine insulated wire elements (<0.3 mm diameter) and carefully calibrated, exhibiting linearity and gain stability better than 2 %.

2.2.1. *Measurement of wave speed*

The presence of any wind drift current can cause a Doppler distortion in any fixed measurements of wave characteristics. Assuming linear dispersion yields a relationship between intrinsic frequency and wavelength (Phillips 1977, p. 38):

$$\omega = \sqrt{gk + Tk^3} \tag{2.1}$$

where T is the water surface tension. The presence of a drift current, u_{drift}, in the same direction as the waves causes the Doppler shift:

$$\omega_p = \omega \frac{c + u_{drift}}{c} \tag{2.2}$$

where ω_p is the observed angular frequency. The magnitude and influence of the drift current will depend of the scale of the wave.

There are three methods typically used in an attempt to remove Doppler distortion and estimate the magnitude of the wind current:

(i) record the wavelength of the waves photographically and compare the observed and intrinsic linear wave frequencies;

(ii) if the waves are monochromatic, the intrinsic and observed wave frequencies can be compared;

(iii) measure the actual speed of travel between two fixed points and use the intrinsic relationship between wavenumber, frequency and speed to close (2.1) and (2.2):

$$c = \frac{\omega}{k}. \tag{2.3}$$

These approaches were pioneered at the IRPHE laboratory in the large-scale facility (Ramamonjiarisoa & Coantic 1976; Coantic *et al.* 1981). During these present studies, the second method was used in the small WRL facility and the third method was used in the large IRPHE facility, the actual speed of travel being determined from the phase lag obtained by cross-correlating wave records between two probes with a spacing of 22 mm.

The following wave field key values are summarized in table 1: the frequency of applied monochromatic waves f_m (column C), the observed peak spectral wave frequency f_p (column D), the intrinsic linear wave speed $c_{intrinsic}$ (column F), the computed wind drift velocity transporting the waves u_{drift} (column G) and the mean wave steepness ak (column H). The value of u_{drift} is listed as zero when it is computed to be less than 0.01 m s^{-1}.

2.2.2. *Measurement of wave field development*

Under conditions of steady wind ($\partial/\partial t = 0$), the development of the wave field is determined by the local spatial gradient of wind–wave energy:

$$\left.\frac{\mathrm{d}E}{\mathrm{d}t}\right|_{\Delta\omega} = \left(c_g + u_{drift}\right) \left.\frac{\partial E}{\partial x}\right|_{\Delta\omega} \tag{2.4}$$

where $\Delta\omega$ is the bandwidth centred around the spectral peak. Conventionally (Wilson *et al.* 1973; Mitsuyasu & Honda 1982; Peirson & Garcia 2008), this is undertaken by fitting the model

$$E(x) = E_0 \mathrm{e}^{\Delta\cdot(x-x_0)} \tag{2.5}$$

to measurements of local energy density E at fetches x close to the point of interest (located at x_0) where Δ is a spatial dimensional growth rate. Then,

$$\frac{\partial E}{\partial x} = \Delta \cdot E. \tag{2.6}$$

For the small WRL tank experiments, the wind–wave conditions were purposefully established to minimize any changes in the surface wave field with fetch. By carefully balancing the wind input to the mechanical waves with the total energy losses of the waves, the conditions of approximately constant energy density can be established yielding $\partial E/\partial x = 0$.

In the large IRPHE tank, wave spectra were measured at three points over a total fetch of 5.3 m encompassing the measurement point. For the mechanically generated non-breaking waves at the lower wind speeds, the wave growth was weak and the local measurements were reconciled with measurements along the entire fetch of the facility.

For all wave cases $\Delta\omega$ was set to span the frequency range from $\omega_p/\sqrt{2}$ to $\sqrt{2}\omega_p$ with $\omega_p = 2\pi f_p$. These frequency ranges were found to encapsulate over 92 % of the total spectral energy of the dominant waves. Two representative examples of the spectral distribution of the wave energy are reported in the figure 1. In the pure wind wave case U7F0 ($U_m = 7$ m s^{-1}), about 93 % of the total spectral energy is supported

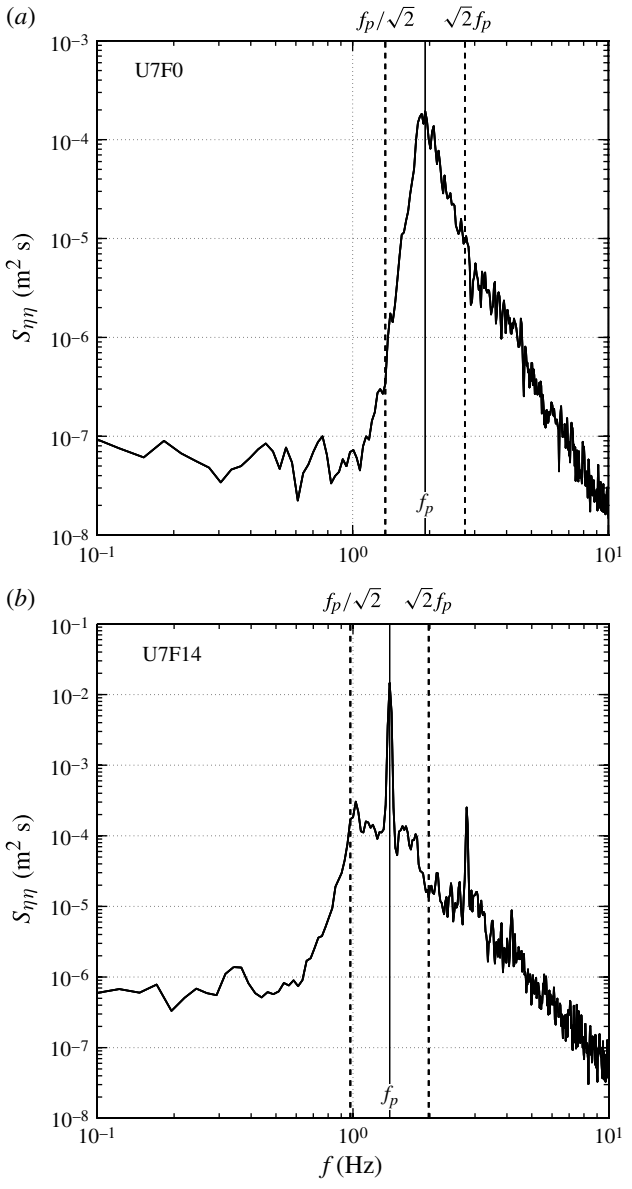

FIGURE 1. Spectra of the water surface elevation signal. (*a*) Pure wind-wave case ($U_m = 7$ m s^{-1}). (*b*) Mechanically generated case ($f_m = 1.4$ Hz, and $U_m = 7$ m s^{-1}). The vertical dotted lines represent the bounds of the frequency range $\omega_p/\sqrt{2} < \omega < \sqrt{2}\omega_p$ where $\omega_p = 2\pi f_p$ is the spectral peak frequency of the dominant waves. This frequency range was found to encapsulate over 92 % of the total spectral energy of the surface elevation for all of the cases studied.

in this frequency range. In the mechanically generated waves case U7F14 ($f_m = 1.4$ Hz, $U_m = 7$ m s^{-1}), more than 94 % of the total energy is encapsulated in this bandwidth. For the pure wind-wave case, it is important to reiterate that the spatial rate of change of wave energy outside of the selected frequency band for any experimental case was

less than 1 % of that measured within the selected band. This demonstrates that no significant nonlinear energy flux occurred from the selected band to waves of lower frequency, thereby validating our approach to determining S_{diss}.

Wave breaking is known to enhance significantly both momentum and energy fluxes from the air to the water (Banner & Melville 1976; Banner 1990; Melville, Veron & White 2002; Makin *et al.* 2007). Therefore, local measurements of the probability of wave breaking were made for this present study. For each measurement case, these probabilities were determined by averaging ensembles of counts of the relative numbers of breaking and non-breaking dominant waves within a given sample time period visually observed to cross the designated measurement point. The probability of observed wave breaking p_b is reported in the table 1, column E. The presence of breaking was determined according to whether the crest was observed to be spilling evidenced by a sharp discontinuity in the forward face slope and ripples radiating rearward from the spilling toe.

2.3. *Measurement of the total stress*

The bulk wind forcing applied in each case is shown in table 1, column B. However, the actual momentum flux that is applied to the surface depends also strongly on the characteristic wave condition (Donelan 1990; Jones & Toba 2001; Makin *et al.* 2007)).

There are two conventional methods of determining total stress, and therefore corresponding wind friction velocity and the air roughness length (Kawamura *et al.* 1981). In the large IRPHE facility, turbulent stress profiles (measured at a series of fixed elevations above the surface) were determined using cross correlations of the horizontal and vertical velocity fluctuations obtained from a hot X-wire probe. Between two sets of needle-shaped prongs, wires of 5 μm diameter and 1.2 mm length were suspended orthogonally at a 45° angle in a vertical plane aligned with the mean wind direction. The wires were connected to two DISA model 55 constant-temperature anemometers. The same calibration method described by Mastenbroek *et al.* (1996) was used except that the calibrations were performed inside the large tank to match the characteristic humidity and temperature values encountered during the present experiments.

The measured turbulent stress profiles demonstrated the existence of a constant flux layer above the water surface within an approximate thickness of 10–20 cm. The values of the total stress were derived from the mean values of the turbulent stress in this layer. The hot X-wire probe was also used to measure the mean wind speed profile in the constant flux layer yielding a logarithmic distribution of the wind speed $U(z)$ (Coantic *et al.* 1981), The air-sided roughness length z_0^a was derived from the logarithmic law $U(z) = (u_*^a/\kappa)\ln\left(z/z_0^a\right)$ using the friction velocity $u_*^a = \sqrt{\tau/\rho_a}$ calculated from the total stress previously determined by cross correlations. The Von Kármán constant κ was set to 0.41.

In the smaller WRL facility, the logarithmic layer was thin making X-wire probe measurements vulnerable to impact of waves on the probe elements. Consequently, the wind stress and air-sided roughness length z_0^a were derived from the logarithmic portions of mean air velocity profiles measured using a 2 mm diameter Pitot tube that could be referenced to the mean water level within ±0.2 mm.

The total stress τ and the air-side roughness length z_0^a values obtained by these methods are shown in columns I and J of table 1. From these values, the wind speed $U_{\lambda/2}$ at $z = \lambda/2$ and the wind speed U_{10} at $z = 10$ m were derived and are reported in columns K and L of table 1.

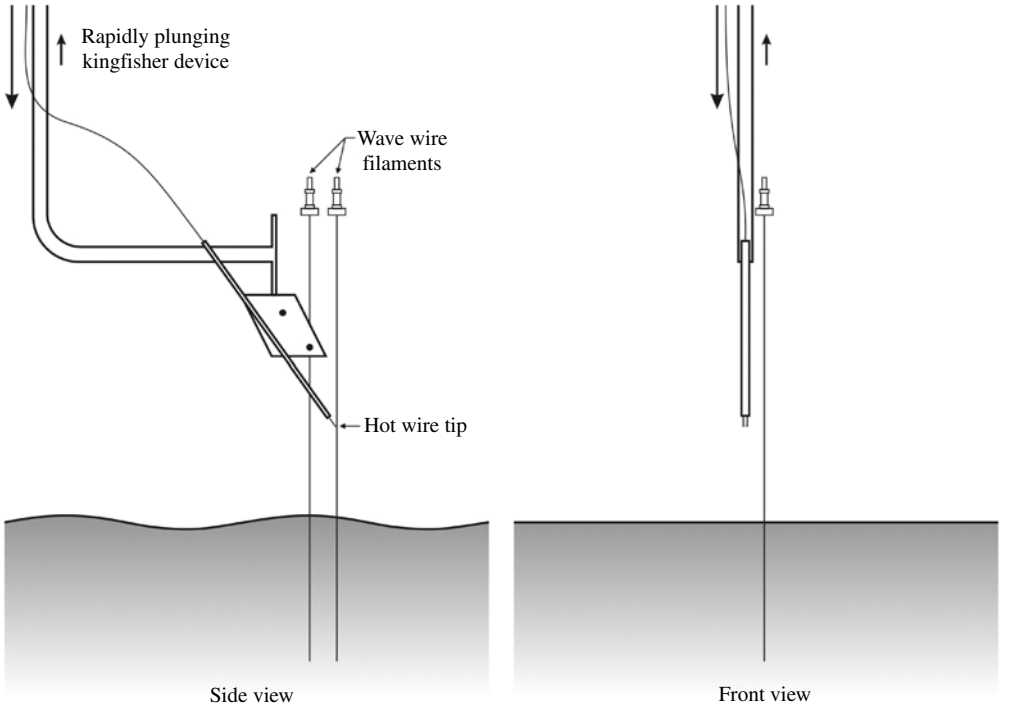

FIGURE 2. A sketch of the physical arrangement of the kingfisher device in the large IRPHE facility. Behind the kingfisher are the two wire probes used to determine wave phase and wave speed. Cross-tank spacing between the kingfisher tip and the upwind wave probe is 5 mm.

2.4. *Measurement of the viscous stress*

Measurements of the interfacial viscous stress are undertaken by measuring the velocity shear within the linear viscous sublayer on the water side or on the air side of the interface. The aqueous sublayer is of physically larger dimension with smaller shear and therefore the surface velocity and, consequently, the wave–coherent tangential stress can also be measured (Banner & Peirson 1998; Peirson & Banner 2003). For the measurements in the small WRL facility, the PIV techniques developed and described in detail by Peirson (1997) were used.

For the measurements in the large IRPHE facility, a new technique using a hot-wire technology coupled with a high-speed linear actuator (Copley Corp., Model XTB 3810; maximum velocity and acceleration are 2.8 m s^{-1} and 300 m s^{-2}, respectively) was developed. A detailed description is available in Grare (2009) and a brief summary is contained here.

The complete device, termed a kingfisher (shown in figure 2) due to its characteristic motion, undertakes a rapid vertical profile downwards from an initial position approximately 120 mm above the mean water surface. Moving with a velocity of 1 m s^{-1}, the kingfisher carries a single 5 μm diameter horizontal hot wire. This hot wire is held transversely relative to the approach flow by a probe mounted at 45° below the horizontal. The probe traverses downwards and through the water surface to a depth of 80 mm. Then the probe is returned to its initial position in the air. The probe is rapidly agitated by the actuator to shake any entrained water from its surfaces and then holds its position in the air for a duration of 10 s to evaporate

any remaining moisture before repeating the cycle. The 10 s delay also ensures that any flow disturbance generated in the air and the water by the kingfisher as it passes through the surface is dissipated prior to any subsequent measurements. The kingfisher was operated in conjunction with the wave probes during the measurements. The width profile of the kingfisher device is small and therefore the air-flow implications for the wave probes were inconsequential. Ring waves are only generated once the kingfisher pierces the surface and it was ensured that the wave probe slope measurements were not contaminated by the ring waves.

A primary challenge associated with this method was to maintain accurate measurements of the velocity in the air without damaging the wire when it impacted the water surface. To avoid physical damage to the wire, the hot-wire overheat ratio was set to 1.2. Nonetheless, the characteristics of the wire slowly changed each time the probe was immersed, leading to a systematic drift in the King coefficients:

$$E^2 = A + B\sqrt{U} \tag{2.7}$$

where E is the potential difference across the wire, U is the measured velocity and A, B are the King coefficients. About 100 dives were performed for each wind–wave condition studied, thus it was not possible to calibrate the wires after each individual dive. Successive calibrations were undertaken, before and after each n measurement ensemble to obtain initial (A_1, B_1) and final (A_n, B_n) King coefficients. Between each calibration, for an individual ith measurement $(1 < i < n)$, the B_i coefficient was linearly interpolated via

$$B_i = B_1 + \frac{(i-1)}{(n-1)}\,(B_n - B_1)\,. \tag{2.8}$$

The value of the A_i coefficient was then adjusted using the mean value of the voltage before each dive E_i^h (after sufficient time had elapsed for the wire to dry) in order to match with the mean value E_1^h before the first dive, where the superscript h denotes the altitude of the upper position of the kingfisher (about 120 mm above the mean surface):

$$A_i = E_i^{h2} + \frac{B_i}{B_1}\left(E_1^{h2} - A_1\right). \tag{2.9}$$

With these adjustments, the absolute error of the measured velocity remained less than 0.2 m s^{-1}. During a dive, the minimum velocity measured by the sensor is the vertical speed of diving (=1 m s^{-1}). Thus, the maximum relative error of the measured velocity was 20 %. Neither the recorded velocities in the viscous sublayer nor the computed tangential stresses showed systematic mean shifts in time.

The exact instant (T_i) when the hot wire impacted the water surface was indicated by an abrupt increase of the voltage across the wire. Therefore,

$$z(T_i) = z_i = \eta(T_i) \Rightarrow \xi_n(T_i) = \xi_n^i = 0 \tag{2.10}$$

where z is the absolute altitude and ξ_n is the normal (perpendicular to the water slope) distance of the probe from the surface. Immediately prior to contact with the surface, a distinctly linear velocity distribution was clearly visible in each velocity profile, indicative of the linear sublayer in the air. Figure 3 shows a single realization of the normalized vertical wind speed profile measured with the kingfisher device, $U^+(z) = U(z)/u_*^a$ as a function of $z^+ = z \cdot u_*^a/\nu_a$, where u_*^a is the friction velocity of the air, and ν_a is the kinematic viscosity of the air. The profile is linear in the very close

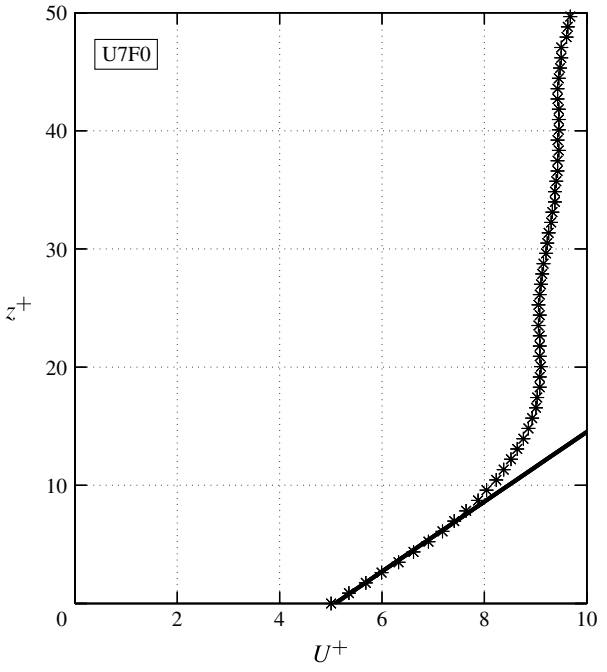

FIGURE 3. Representative wall-normalized velocity profile obtained in large IRPHE facility from the kingfisher and shows a near-instantaneous determination of the tangential stress.

vicinity of the water surface. $z^+ = 8$ is equivalent to a distance of about 0.5 mm for this example.

The constant speed of diving $w_s = 1$ m s^{-1} permitted relating the time to the height of the probe relative to the interface. The surface viscous stress was determined from

$$\tau_{visc} = \mu_a \left. \frac{\partial U_t}{\partial \xi_n} \right|_{\xi_n = 0} \tag{2.11}$$

where μ_a is the dynamic viscosity of the air and U_t is the tangential velocity in a wave-following frame of reference. The tangential velocity U_t is computed from the vectorial equation:

$$\boldsymbol{U} = U_t \boldsymbol{t} + U_n \boldsymbol{n} + w_s \boldsymbol{z} \tag{2.12}$$

where $(\boldsymbol{t}, \boldsymbol{n})$ are the local tangential and normal vectors of the surface when the probe impacts the surface. The tangential velocity U_t is the positive root of the quadratic equation:

$$U_t^2 + 2U_t w_s \sin\theta + w_s^2 + U_n^2 + 2w_s U_n \cos\theta - U^2 = 0 \tag{2.13}$$

where $\theta = -\arctan(\partial\eta/\partial x)$ and U_n was assumed to be equal to $(\partial\eta/\partial t)\cos\theta$. The kingfisher instrument sampling frequency was 20 kHz, which provided a time step of 50 μs, yielding to a vertical resolution of 50 μm. With the wave probe pair mounted adjacent to the kingfisher with a cross-tank separation of 5 mm, the contact of the probe with the water surface was related to the phase of the propagating wave forms. For each test case, about 100 individual kingfisher dives were completed. The nature of the operation of the kingfisher was that these dives were randomized in terms of

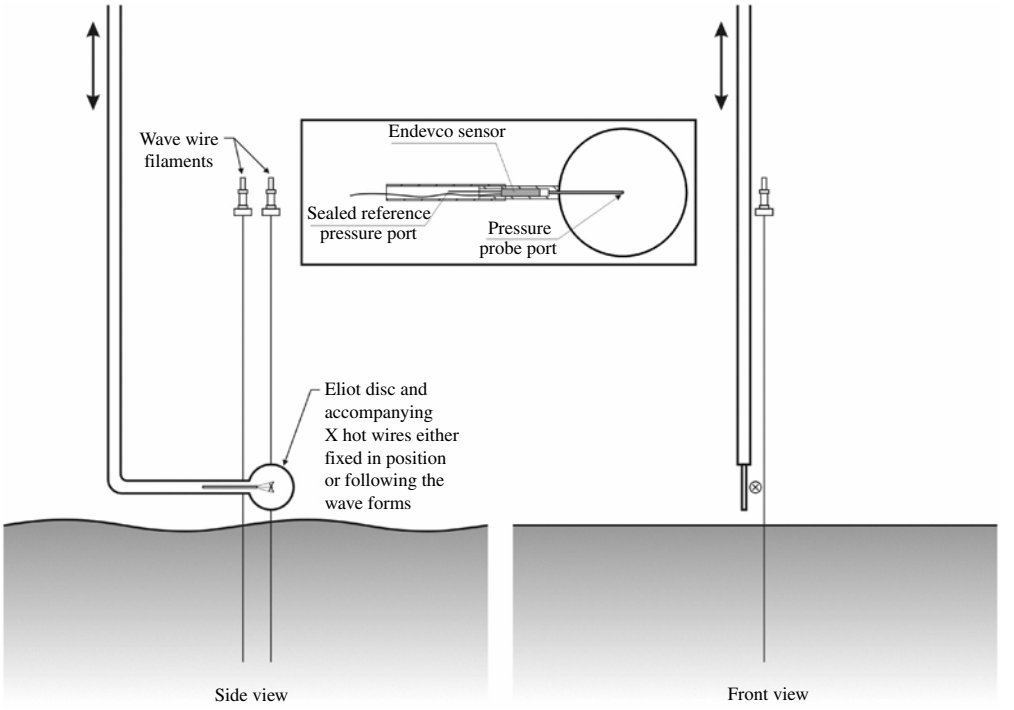

FIGURE 4. A sketch of the physical arrangement of the hot-wire/pressure probe mounted on the wave-follower in the large IRPHE facility. The hot X-wire is mounted between the Elliott pressure disc and the two wave gauges. The inset figure is a sketch of the pressure probe. The pressure sensor is located 25 mm downwind from the centre of the Elliott disc. Cross-tank spacing between each instrument is 5 mm.

wave phase and therefore continuous distributions along representative waves could be determined (see figure 8.1 in Grare (2009)).

The mean tangential stress measurements for each test case are shown in table 1, column M.

2.5. *Direct measurement of form drag*

2.5.1. *Measurement of static pressure*

Static pressure measurements were undertaken, in the large IRPHE facility, using the pressure probe disc developed by Elliott (1970, 1972*a*,*b*) and a piezo-resistive pressure transducer sensor. The primary improvement in the present probe is that the pressure sensor was placed as close as possible to the sensing ports (within 25 mm; see figure 4).

The disc probe was fabricated with a mix of epoxy resin and micro hollow glass balls under vacuum using a shaped mould. The disc is 4 cm diameter, its thickness is between 1.85 and 2.1 mm and the diameter of its sensing ports is 0.5 mm. The pressure port routing tube has a 0.5 mm internal diameter. The piezo-resistive sensor is the model 8507C-1 from the Endevco Corporation, 2.3 mm in diameter and 12 mm long. Its sensitivity is 30 mV kPa^{-1} for an operating range of 7 kPa. Its small size allows the sensor to be placed inside the tube supporting the disc. The air volume contained between the sensing probe holes and the pressure sensor is then reduced to

less than 50 mm^3. The natural resonant frequency of this sensor is 55 kHz, yielding a variation of sensitivity in the transducer of less than 4 % up to 10 kHz. In the present case, this alleviates the need for frequency calibration (Donelan *et al.* 2005), required by larger-scale pressure transducers.

Apparent static pressure perturbations can be created by oblique velocities that induce dynamic pressures or by the vertical motion of the wave-follower. Using the Elliott disc ensured that static pressure error relative to the dynamic pressure remained less than 5 % for a yaw angle less than 10° (Elliott 1970, 1972*a*,*b*). For wind waves generated for a centreline wind speed of 8 m s^{-1}, measurements located 5 cm above the mean water level using a hot X-wire probe showed that the angle of attack of the flow remains within 10° for greater than 95 % of the time.

Perturbations induced by the movement of the probe could potentially contaminate the static pressure measurements. The precautions taken to minimize their impact are as follows.

(*a*) Inertial effect of the air contained in the connecting tubes; the pressure sensor was placed less than 25 mm away from the pressure probe ports. The inertial effect of the accelerated air contained in the tube was negligible in comparison with the static pressure variations recorded (about 1 Pa). Furthermore, the reference pressure port of the transducer was sealed to reduce the volume of air on the reference side of the transducer to less than 10 mm^3. Although the corresponding correction of the accelerated air–volume was negligible, the sealing of the reference pressure port implies that the low-frequency atmospheric fluctuations were recorded. These fluctuations were removed by high-pass filtering (0.3 Hz) of the raw pressure signal.

(*b*) Acceleration of the transducer diaphragm; the diaphragm of the transducer was mounted in a vertical plane making it not sensitive to the vertical acceleration of the probe.

(*c*) Displacement within the vertical atmospheric pressure gradient. Fluctuations of the static pressure are induced by vertical displacements of the probe within the vertical gradient of the atmospheric pressure due to the variations of the hydrostatic pressure. In principle, this pressure term is out of phase with the surface elevation and therefore does not contribute to the pressure–slope correlation. Detailed analysis showed that for the real data, the values of the pressure–slope correlations increase by less than 2 % if the hydrostatic pressure displacement correction is applied.

The frequency response of the assembled 'Elliott disc/transducer unit' was compared with a pressure transducer without the Elliott disc. A sound generator was activated at one end of a closed cylinder with the two probes inside. The speaker was stimulated by a signal generator with a sinusoidal waveform for frequencies varying from 0.1 Hz to 10 Hz. The phase lag of the assembled instrument remained less than 0.5° with an attenuation less than 4 %.

As observed by others (Latif 1974; Papadimitrakis, Hsu & Street 1984; Banner 1990), the driving mechanism and the displacement of the wavemaker induce large acoustic pressure fluctuations inside the wave tank. For this investigation, this issue was avoided by recording the wavemaker displacements and analysing the acquired data only when the wavemaker was turned off (see Mastenbroek *et al.* 1996).

2.5.2. *Positioning of the pressure sensor*

The complete static pressure probe was mounted on the linear actuator used for the kingfisher. The pressure probe was located adjacent to the X-wire with a cross-channel spacing of 5 mm (figure 4). The actuator was operated in two different modes: static and wave-following. In static mode, a constant voltage ensured that the probe remained within 18 μm of a specified constant position above the mean water level.

In the wave-following mode, the wave gauge output signal was connected to the actuator command via a signal conditioning which controlled the gain, sensitivity, speed and acceleration of the following device. The sensitivity of the system was adjusted to match optimally the wave gauge sensitivity resulting in an accurate response of the actuator to the elevation of the surface.

However, the part of the wave gauge signal generated by the high-frequency waves introduced an error response of the actuator leading to potential vibrations of the structure supporting the wave follower. These vibrations generated errors in the vertical position of the probe and noise perturbations that were recorded by the pressure probe. To avoid this problem, the parameters of the actuator feedback loop were adjusted to filter out these high-frequency components. A linear displacement sensor monitored the actual actuator displacements with a precision better than ±50 μm. The final tracking error was less than 10 % in amplitude and less than 7° lag in phase for frequencies up to 3 Hz. The performances of the wave-follower system, with all of the technical details are described in Grare (2009).

2.6. *Indirect measurement of static pressure*

Deardorff (1967) developed equations of the momentum flux from the air to water between a moving surface and a constant height above the mean water level. However, his formulation cannot be applied to wave-follower measurements. These equations have been developed further to express the momentum fluxes in the wave-follower frame (see Appendix for the detailed derivation).

The components of the velocity and pressure are decomposed into mean, wave-induced and turbulent parts. The mean part of a time-dependent function $q(t)$ is defined by (Mastenbroek *et al.* 1996)

$$\overline{q} = \frac{1}{T}\int_0^T q(t)\,\mathrm{d}t. \tag{2.14}$$

Assuming that a part of q is induced by N waves of period τ, the wave induced part of q is defined by

$$\tilde{q}(t) = \frac{1}{N}\sum_{n=1}^{N} q\,(t + n\tau) - \overline{q}. \tag{2.15}$$

The remaining fluctuating part of q is the turbulent part defined by

$$q''(t) = q(t) - \overline{q} - \tilde{q}(t). \tag{2.16}$$

Assuming that the transverse velocity of the air flow is negligible and the wave field is two-dimensional, the total stress τ is defined by the sum of three components (pressure–slope correlation, a term due to wave-follower motion and a viscous term) expressed at the constant wave-following height $\xi = h$ (see Appendix):

$$\tau = \tau_p^h + \tau_a^h + \tau_v^h \tag{2.17}$$

where

$$\tau_p^h = \overline{\tilde{p}\frac{\partial \eta}{\partial x}}\bigg|_h \tag{2.18}$$

$$\tau_a^h = -\rho_a \overline{\tilde{u}\tilde{w}}\big|_h - \rho_a \overline{u''w''}\big|_h + \rho_a \overline{\tilde{u}\frac{\partial \eta}{\partial t}}\bigg|_h + \rho_a \overline{\tilde{u}^2\frac{\partial \eta}{\partial x}}\bigg|_h + \rho_a \overline{u''^2\frac{\partial \eta}{\partial x}}\bigg|_h + 2\rho_a \overline{u}\,\overline{\tilde{u}\frac{\partial \eta}{\partial x}}\bigg|_h \tag{2.19}$$

$$\tau_v^h = \mu_a \frac{\partial \overline{u}}{\partial \xi}\bigg|_h + \mu_a \overline{\left(\frac{\partial \eta}{\partial x}\right)^2 \frac{\partial \tilde{u}}{\partial \xi}}\bigg|_h + \mu_a \overline{\left(\frac{\partial \eta}{\partial x}\right)^2}\frac{\partial \overline{u}}{\partial \xi}\bigg|_h - 2\mu_a \overline{\frac{\partial \eta}{\partial x}\frac{\partial \tilde{u}}{\partial x}}\bigg|_h$$
$$- \mu_a \overline{\frac{\partial^2 \eta}{\partial x^2}\tilde{u}}\bigg|_h - \mu_a \overline{\frac{\partial^2 \eta}{\partial x^2}u''}\bigg|_h - \mu_a \overline{\frac{\partial^2 \eta}{\partial x^2}}\,\overline{u}\bigg|_h . \tag{2.20}$$

Equation (2.17) can also be transformed into

$$\tau_p^h = \tau - \tau_a^h - \tau_v^h . \tag{2.21}$$

Assuming that viscous effects are insignificant at elevation h above the surface, the RHS of (2.21) only depends on the total stress, the local velocities and the surface elevation. By extrapolation of τ_p^h to the surface, this provides an alternative indirect method of determining form drag without relying on direct static pressure measurements which are vulnerable to signal contamination as described previously. In general, velocity measurements are more straightforward and reliable than static pressure measurements.

3. Results and discussion

3.1. *Stress partition*

Figure 5 shows the form drag normalized by the total wind stress for all measurements presented in table 1. The values obtained from measurements of the viscous stress are computed using (1.5). Several observations can be made. The two sets of tangential stress measurements show reasonable consistency and systematic behaviour as a function of wave steepness. This consistency, their ability to capture linear behaviour adjacent to the surface and the simplicity of the measurement provide clear evidence of their reliability in determining the surface tangential stress. The form drag measurements are in reasonable agreement with the tangential stress measurements although some cases exhibit implausibly large form drag values. This issue can be explained by the fact that the form drag is estimated by extrapolation at the surface of the pressure–slope correlations.

The upper panels of figures 6 and 7 provide two examples of the three potential methods of measuring the form drag. Far from the surface, both the fixed and the following measurements are in reasonable agreement, although fixed measurements do produce absolute wave–coherent pressure fluctuations that are systematically smaller than those determined when the wave-follower data are used. Further, the indirect calculation of the static pressure does appear to yield higher wave–coherent pressure variations than obtained by the static pressure probe itself. The near surface vertical pressure gradients are substantial and show that the use of a single static pressure measurement is not appropriate. As indicated by the fits in figures 6 and 7 (upper panels), for the fixed probe measurements, the pressure/wave slope correlation varies linearly rather than exponentially away from the surface.

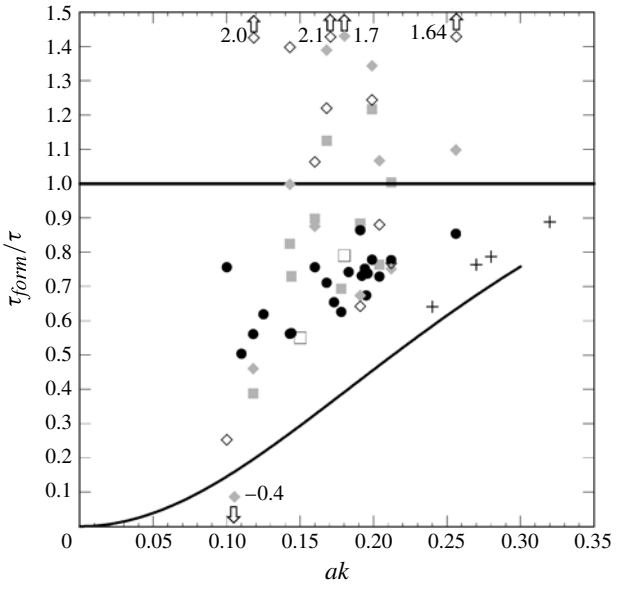

FIGURE 5. Comparison of form drags as normalized proportions of the total wind stress obtained during this study as a function of wave steepness. Tangential stress measurements have been transformed to normalized form drags using (1.5): plus signs, obtained from viscous measurements using PIV techniques in the small WRL facility (Peirson *et al.* 2012); solid circles, obtained from viscous measurements using the kingfisher in the large IRPHE facility (Grare 2009); hollow squares, Mastenbroek *et al.* (1996); solid grey squares, linear extrapolations to mean water level of fixed static pressure data (Grare 2009); solid grey diamonds, linear extrapolations to moving water surface of wave follower-measured static pressure data (Grare 2009); hollow diamonds, linear extrapolations to moving water surface of wave follower indirectly derived static pressure data (Grare 2009); solid curve, approximate mean curve estimates obtained from net measurements of wave growth by Peirson & Garcia (2008).

However, the key feature causing this systematic overestimate of the surface pressure is shown in the wave-following measurements in the lower panels of figures 6 and 7. In the vicinity of a distance $k\xi \sim 0.5$ ($\xi \sim \lambda/12.5$) there is a distinct change in the near-surface pressure field such that the wave–coherent pressure fluctuations decrease rather than increase in proximity to the surface. We do not believe that this behaviour has been observed previously although the numerical model results of Mastenbroek *et al.* (1996, figure 11) with higher-order closure anticipate such behaviour with distance above the mean surface. Banner & Peirson (1998) and Reul, Branger & Giovanangeli (2008) show strong separation in the wakes of these wind-forced waves on a vertical scale of twice the wave amplitude which is approximately $k\xi = 0.5$ for these conditions. It may be that strong spatial gradients in the vertical velocity have a significant impact on the vertical pressure gradients. Further investigation is warranted to resolve these issues.

In spite of the obvious differences between the local values of wave–coherent surface pressure between the direct and indirect methods, the simplicity of the indirect method and its promising performance warrants further investigation, particularly for potential application in open ocean conditions.

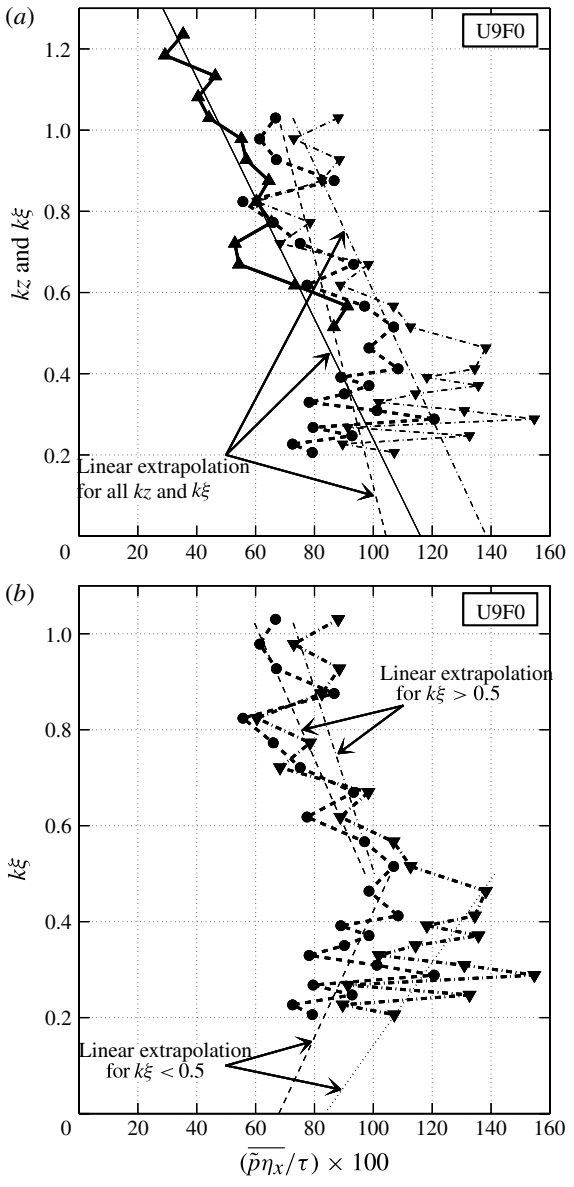

FIGURE 6. Vertical profiles of normalized pressure/wave slope correlation, and extrapolations of the normalized form drag at the water surface for the case U9F0. (*a*) Comparison of fixed, direct follower and indirect methods of determining form drag. (*b*) Lower panel shows the change in the pressure–slope correlation at height h that occurs at approximately $k\xi = 0.5$: solid line with upward triangle, fixed static pressure measurements; solid thin line, linear extrapolation of the fixed static pressure measurements to the mean water level; dashed line with solid circle, wave-following direct static pressure measurements; dashed thin line, linear extrapolation of the wave-following direct static pressure measurements to the surface; dash-dotted line with downward solid triangle, wave-following indirect static pressure estimates; dash-dotted thin line, linear extrapolation of the wave-following indirect static pressure estimates to the surface.

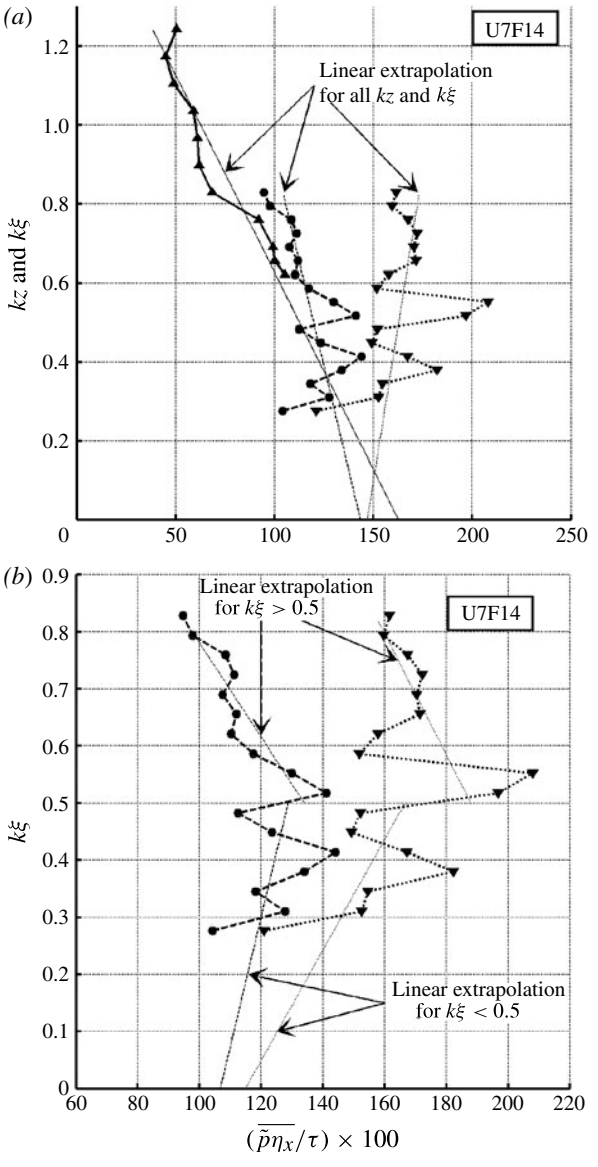

FIGURE 7. Vertical profiles of normalized pressure/wave slope correlation, and extrapolations of the normalized form drag at the water surface for the case U7F14. (*a*) Comparison of fixed, direct follower and indirect methods of determining form drag. (*b*) The change in the pressure–slope correlation at height h that occurs at approximately $k\xi = 0.5$: solid line with upward triangle, fixed static pressure measurements; solid thin line, linear extrapolation of the fixed static pressure measurements to the mean water level; dashed line with solid circle, wave-following direct static pressure measurements; dashed thin line, linear extrapolation of the wave-following direct static pressure measurements to the surface; dash-dotted line with downward solid triangle, wave-following indirect static pressure estimates; dash-dotted thin line, linear extrapolation of the wave-following indirect static pressure estimates to the surface.

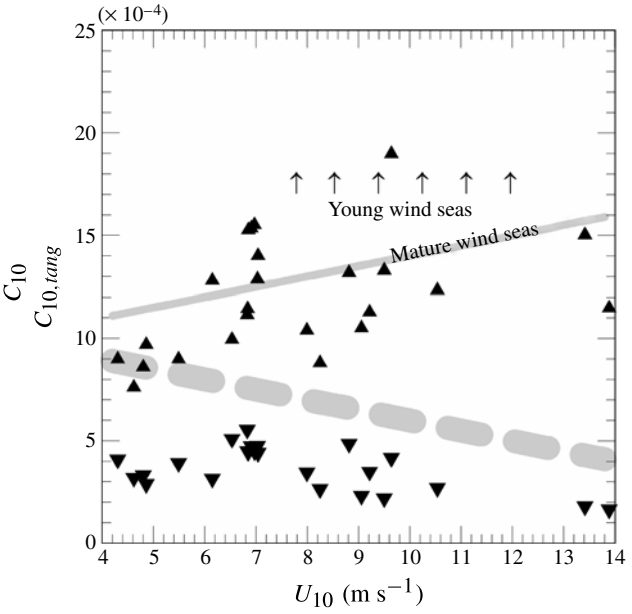

FIGURE 8. Comparison of tangential stresses with Banner & Peirson (1998): upward pointing triangles, C_{10}; downward pointing triangles, $C_{10,tang}$; solid thin grey line indicates representative mature sea total drag coefficients; dashed heavy grey line indicates tangential drag coefficients determined by Banner & Peirson (1998).

We now explore the implications of the previous results in determining wind input, wave growth and losses from the wind-forced wave fields. We start by comparing the present results with the measurements of Banner & Peirson (1998). This is shown in figure 8 where the two grey lines indicate the total and tangential drag coefficients determined by Banner & Peirson (1998).

$$C_{10} = \frac{\tau}{\rho_a U_{10}^2} \quad \text{and} \quad C_{10,tang} = \frac{\tau_{tang}}{\rho_a U_{10}^2}. \tag{3.1}$$

Their laboratory total drag data lie slightly below the solid thin heavy grey line in figure 8, approaching it as the fetch increases (see the upper panel of figure 12 in Banner & Peirson (1998)).

Banner & Peirson (1998) tangential drag results at their longer fetches lie in the vicinity of the dashed heavy grey line shown in figure 8, differing from the present results by approximately a factor of two. To the best of the authors' knowledge, Banner & Peirson (1998) and this present study are the only two systematic investigations of tangential drag coefficients. Consequently, there is no other direct independent evidence available to explain this difference but we offer the following potential explanation.

The measurement techniques used in the small WRL facility for this present study and those of Banner & Peirson (1998) are identical. Yet the tangential drag coefficients yielded by the present are a factor of two smaller than Banner & Peirson (1998). The form drags as normalized proportions of the total wind stress obtained from this study are very similar to those measured by Banner (1990) for well-developed waves. Consequently, the relatively high level of wave development of the present study

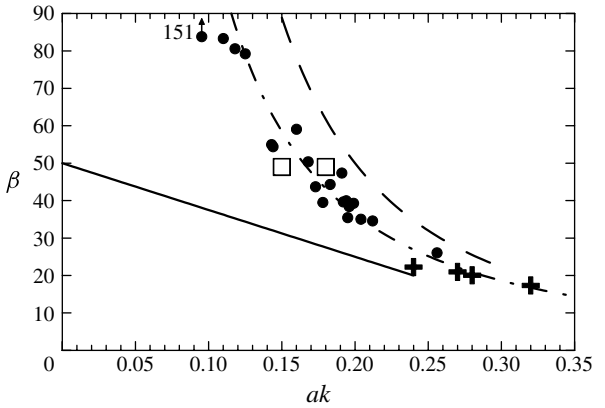

FIGURE 9. Normalized wind-energy input rate expressed as function of mean wave steepness. Hollow squares are data from Mastenbroek *et al.* (1996), solid circles are obtained from viscous measurements using the kingfisher in the large IRPHE facility (Grare 2009) and the crosses are values measured using PIV techniques in the small WRL facility (Peirson *et al.* 2012). The dashed line indicated the theoretical limit $\beta = 2/(ak)^2$ and the solid line indicates the mean values of net wave growth determined by Peirson & Garcia (2008). The dash-dotted line indicates the best power fit of the data: $\beta = 2.56(ak)^{-1.65\pm0.11}$.

relative to those investigated by Banner & Peirson (1998) who observed a systematic decrease in tangential stress with very short fetch may be a plausible explanation. For much more developed waves (mechanically generated or at fetches seven times greater than the maximum considered by Banner & Peirson (1998)), the tangential stress may continue to fall to the levels observed during the present experiments. A new exciting possibility is the potential application of the kingfisher under field conditions. Nonetheless, a primary conclusion of Banner & Peirson (1998) remains robust: significant levels of tangential stress persist in the presence of well-developed waves under moderate wind forcing.

3.2. *Wind input*

Surface velocities of wind forced waves can be composed as the sum of the wave orbital component and a surface drift of approximately 0.3 u_*^a, with a surface rupture at the toes of spilling regions (Banner & Phillips 1974; Wu 1975; Peirson & Banner 2003; Peirson *et al.* 2012). For friction velocities at moderate wind speeds, the surface velocities are typically less than 10 % of the wind velocities just a few millimetres above the surface. When these factors are coupled with the microscopic thickness of the rapidly moving air-side viscous sublayer, the present investigations found that robust determination of water surface velocities from air velocity at the surface as measured from the kingfisher technique was presently unattainable. Therefore, this present analysis has had to progress on the assumption that the corresponding wave–coherent tangential stresses in the large IRPHE tank make a negligible contribution to the wind input. For the data gathered in the small WRL tank, the computed wave–coherent tangential stress contribution was found to be negligible (Peirson *et al.* 2012).

The corresponding wave drag values (equation (1.7)) can be normalized as a wind input rate β (equation (1.8)) to yield the distribution shown in figure 9. The collapse of the data with the steepness is remarkable, particularly in view of the scatter in

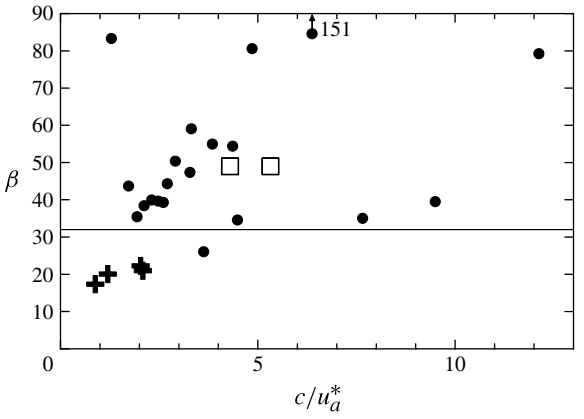

FIGURE 10. Normalized wind-energy input rate expressed as function of wave age. Hollow squares are data from Mastenbroek *et al.* (1996), solid circles are obtained from viscous measurements using the kingfisher in the large IRPHE facility (Grare 2009) and the crosses are values measured using PIV techniques in the small WRL facility (Peirson *et al.* 2012). The solid line indicates the conventional mean value of Plant (1982).

conventional presentations of such data (e.g. Plant 1982, figure 2) and the raw viscous-derived form drags expressed as normalized proportions of the total wind stress (figure 5).

These results show a strong finite amplitude effect that has not been anticipated by previous investigators except for Peirson & Garcia (2008). The mean curve of the wind input data lies above the mean curve obtained by Peirson & Garcia (2008) but bounded above by the theoretical limit $\beta = 2/(ak)^2$ that assumes that the form drag cannot exceed the total stress. The levels are stronger than anticipated by most other investigators and lie within the limits determined by Plant (1982) above a mean steepness of $ak = 0.17$. From (1.1), (1.2) and (1.8), S_{in} can be expressed as follows:

$$S_{in} = \tfrac{1}{2}\sqrt{g}a^2k^{3/2}\beta\rho_a\left(u_*^a\right)^2. \tag{3.2}$$

From figure 9, the best fit is $\beta = 2.56(ak)^{-1.65\pm0.11}$ where the uncertainty in the exponent of ak was determined at 90 % confidence. Substituting the fitted result into (3.2) yields

$$S_{in} = 1.28\sqrt{g}a^{0.35\pm0.11}k^{-0.15\pm0.11}\rho_a u_*^{a2} \tag{3.3}$$

with a correlation coefficient over 0.97 and where the ordering of the errors in the exponents must be correlated to maintain non-dimensionality. It is noted that this expression spans conditions $4.3 < U_{10} < 13.9$ m s^{-1} and therefore representative of moderate wind conditions. Owing to non-dimensionalizing interactions between wave steepness and wave properties defined by linear theory, a myriad of alternative non-dimensional forms of (3.3) can be developed that include (1.8) and (1.9). Equation (3.3) maintains non-dimensionality with reference to as few wave properties as possible.

Figure 10 shows the present data β in the more conventional form as a function of wave age c/u_a^*. No systematic collapse of the data can be observed indicating the overriding importance of wave steepness in determining the wind input even

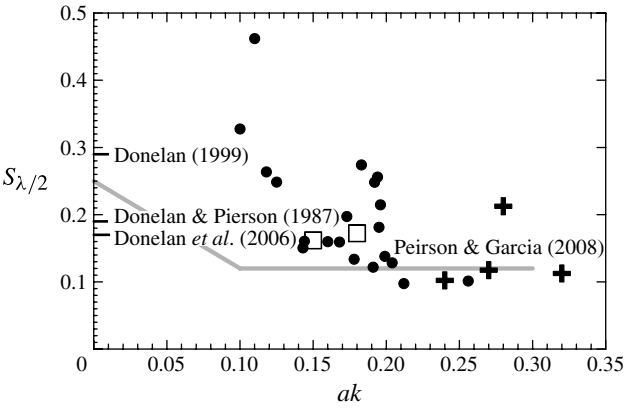

FIGURE 11. Normalized wind-energy input rate, expressed as Jeffreys sheltering coefficients (equation (1.9)), as a function of mean wave steepness. Hollow squares are data from Mastenbroek *et al.* (1996), solid circles are obtained from viscous measurements using the kingfisher in the large IRPHE facility (Grare 2009) and the crosses are values measured using PIV techniques in the small WRL facility (Peirson *et al.* 2012). The grey line indicates the approximate mean values determined by Peirson & Garcia (2008) based on measurements of net wave growth. Solid lines at ordinate axis indicate sheltering coefficients determined by Donelan & Pierson (1987), Donelan (1999) and Donelan *et al.* (2006).

though the wave speeds approach 40 % of $U_{\lambda/2}$ (wind speed at altitude $z = \lambda/2$). The present data are not sufficiently extensive to determine the influences of wave age on normalized wind input.

We investigated other possible non-dimensional presentations of the form drags as normalized proportions of the total wind stress and the normalized wind input term as functions of the wave Reynolds number $aU_{\lambda/2}/\nu_a$, the roughness Reynolds number $z_0^a U_{\lambda/2}/\nu_a$ or the non-dimensional fetch $Xg/U_{\lambda/2}^2$, but the data did not collapse systematically as a function of these non-dimensional variables.

In view of the comments of Phillips (1985, foot of p. 510), some might find such strong normalized levels of wind input at low steepness objectionable with the Plant (1982) normalization of $\beta = 32 \pm 16$, independent of mean wave steepness. As will be shown subsequently, these results are consistent with several other studies. Specifically, Jeffreys sheltering coefficients as determined by Donelan and his collaborators (Donelan 1999; Donelan & Pierson 1987; Donelan *et al.* 2006) are shown in comparison with the present data in figure 11.

Remembering that, in each case, the Donelan values reflect mean sheltering coefficients without consideration of the possible role of wave steepness, the strength of wind input determined during this present investigation is similar in magnitude to those determined independently on the basis of pressure measurements in the air. Given that the wave age and wind forcing conditions of the Donelan investigations are not very different from this present study, the consistency between these studies is reassuring. Nonetheless, the collapse of the data in figure 9 is much more systematic than that found in figure 11. We investigated the presentation of the normalized wind-energy input rate, expressed as Jeffreys sheltering coefficients as a function of the wave age c/u_*, but the data did not collapse systematically showing that no apparent functionality is found between these two variables.

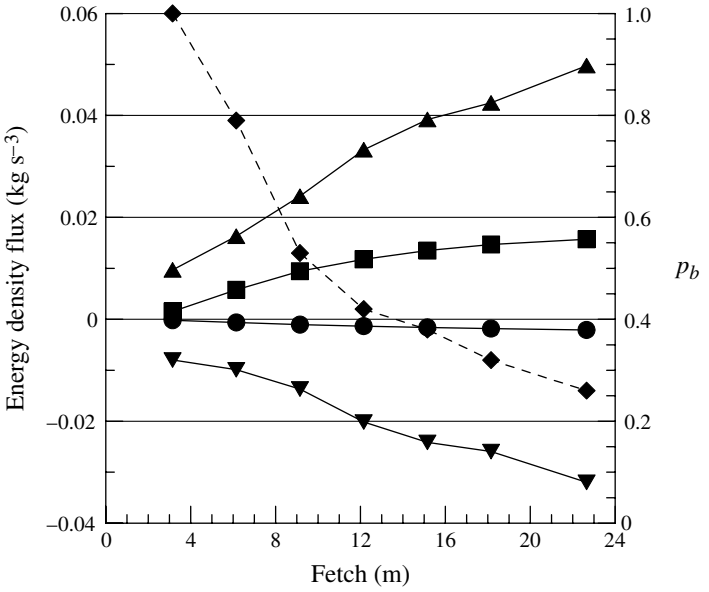

FIGURE 12. Energy budget for wind waves in the large IRPHE facility at 7 m s^{-1} wind speed as a function of fetch: squares, dE/dt; upward pointing triangles, S_{in} (from viscous measurements using the kingfisher); circles, S_{visc}; downward pointing triangles, S_{attn}. Also shown are the corresponding wave-breaking probabilities P_b indicated by the right-hand scale as diamonds.

3.3. *Wave field development and wave attenuation*

Summaries of the total wind-energy input S_{in} in comparison with the other terms in (1.3), (1.4) and (1.10) measured in the large IRPHE wind–wave facility are presented in figures 12, 13 and 14 where $S_{attn} = (dE/dt)|_{\Delta\omega} - S_{in} - S_{visc}$. It can be observed that all quantities form a systematic pattern as a function of fetch, wind forcing and, to a lesser extent, to the wave characteristics. Figures 12–14 also show the probability of breaking for each experimental case.

There are systematic and large differences between the wind input and consequent net wave growth (or attenuation) implying a significant energy loss from the wave field even for conditions in which none of the dominant waves were observed to break. Specifically, for the cases of non-breaking mechanically generated waves, there is a substantial S_{attn} term which is significantly larger than the (near-)negligible viscous losses. As discussed earlier, there is some uncertainty regarding the precise magnitude of the viscous losses but they are inconsequential to the quantitative conclusions of this investigation. At short fetch, when the dominant wave components are in the range of 5–20 cm, energy wave transfer to parasitic capillaries (which then dissipate rapidly) may be larger than the direct viscous dissipation by the dominant waves (Longuet-Higgins 1992; Zhang 2002). This may explain some wave dissipation for non-breaking cases. In our study, six cases present dominant wavelengths smaller than 20 cm. Five of them exhibit a breaking probability greater than 42 %. For these cases, the dissipation rate by generation of capillaries is expected to be small compared with the dissipation rate by breaking. Hence, only one case presents non-breaking waves of wavelengths smaller than 20 cm, and in this case, a significant part of the dissipation could be due to parasitic capillaries riding on lee face of short gravity waves.

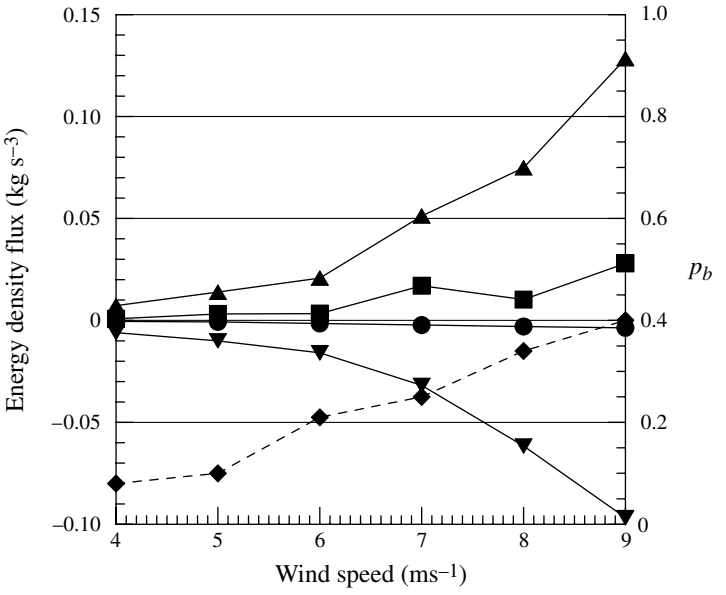

FIGURE 13. Energy budget for wind waves in the large IRPHE facility at 28 m fetch as a function of wind speed: squares, dE/dt; upward pointing triangles, S_{in} (from viscous measurements using the kingfisher); circles, S_{visc}; downward pointing triangles, S_{attn}. Also shown are the corresponding wave-breaking probabilities P_b indicated by the right-hand scale as diamonds.

3.3.1. *Wave–turbulence interactions*

Normalized wave attenuation rates β_{attn} can be computed in a form of (1.8):

$$\frac{S_{attn}}{\omega E} = -\beta_{attn}\frac{\rho_a}{\rho_w}\left(\frac{u_*^a}{c}\right)^2. \tag{3.4}$$

The β_{attn} values are shown as a function of wave steepness in figure 15. Breaking and non-breaking wave cases are distinguished in this figure by the respective symbols. The degree of collapse is remarkable in this normalization. However, there are three data points which do not fit the overall pattern and deserve special comment.

The first is a non-breaking case exhibiting negative normalized attenuation (U4F10, $ak = 0.125$, $\beta_{attn} = -19.4$). As shown in figure 14, for this experimental case, the wind input is weak and comparable in magnitude with other constituent quantities. Reliable determination of β_{attn} is compromised by the small magnitude of the measured quantities relative to the inherent measurement errors. This conclusion is supported by the behaviour of corresponding cases of higher wind forcing (U7F10 and U10F10). Although in these cases, breaking of the dominant waves was also not observed, the corresponding determinations of β_{attn} sit naturally amongst the other data.

There are two other cases which exhibit very high normalized attenuation rates (U4F14, $ak = 0.204$, $\beta_{attn} = 285$ and U7F14, $ak = 0.256$, $\beta_{attn} = 61$). In these specific tests, the overall breaking behaviour differed from all other experimental cases: there was no breaking of the monochromatic waves along the tank as they developed under the influence of wind. However, immediately upwind of the point of measurement, the monochromatic waves in these two cases began to break, releasing the accumulated wind input acquired during their passage along the tank. This wind-forced behaviour

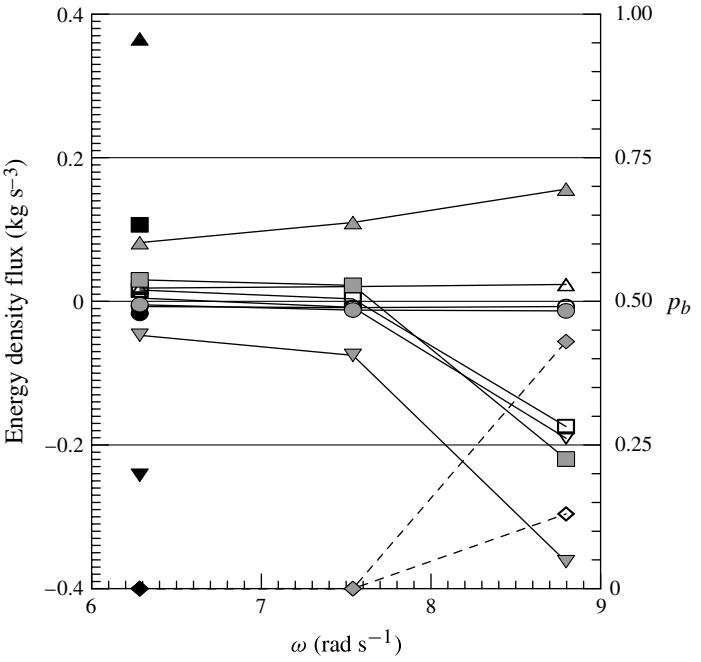

FIGURE 14. Energy budget for monochromatic waves in the large IRPHE facility as a function of wind speed and wave frequency: hollow symbols, $U_m = 4$ m s^{-1}; grey symbols, $U_m = 7$ m s^{-1}; solid symbols, $U_m = 10$ m s^{-1}; squares, dE/dt; upward pointing triangles, S_{in} (from viscous measurements using the kingfisher); circles, S_{visc}; downward pointing triangles, S_{attn}. Also shown are the corresponding wave-breaking probabilities P_b indicated by the right-hand scale as diamonds.

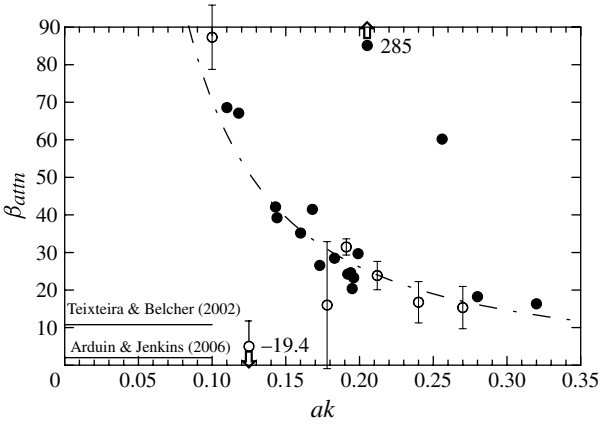

FIGURE 15. Normalized energy loss as a function of wave steepness. Hollow circles are non-breaking waves and solid circles are breaking wave cases. Corresponding estimates by Teixeira & Belcher (2002) and Ardhuin & Jenkins (2006) are shown as solid lines on the ordinate axis. The dash-dotted line indicates the best power fit of the data $\beta_{attn} = 2.62(ak)^{-1.43\pm0.21}$.

is similar to that observed in the highest steepness cases measured by Mitsuyasu & Honda (1982) and shown in their figure 9. For non-wind-forced conditions, this pattern is similar to group behaviour observed by Rapp & Melville (1990), Drazen *et al.* (2008) and Tian *et al.* (2010) and, in which there is a sustained, spatially localized convergence of energy within the wave field leading to subsequent breaking and energy dissipation (Banner & Peirson 2007). Note that the measurement itself, of course, does not contribute to the breaking. The wave probes are constructed with very fine elements. While small ring waves can occasionally been observed radiating from the frame supports, these are tiny and insufficient to trigger the large-scale breaking that was observed.

These results indicate potential characteristic gravity-scale breaking behaviours in the open ocean. Some wave scales can be maintained in a near-saturated state, in which the waves remain in a quasi-equilibrium between the wind input, subsurface dissipation and development. Other, lower-frequency scales can steadily accumulate input energy without breaking to a critical point when rapid, local release of energy occurs.

An unanticipated outcome of these present results is the normalized intensity of the wave attenuation. Although Belcher *et al.* (1994, p. 148) determined that turbulent attenuation of wind-forced waves could be so strong that waves might not grow, we did not anticipate such strong attenuation in our data. Nonetheless as shown in figure 15, the levels of normalized attenuation are found to be systematically high, particularly at low steepnesses. The levels anticipated by Teixeira & Belcher (2002) and Ardhuin & Jenkins (2006) are also shown. Obvious care needs to be taken when extrapolating these results to field conditions and the premises assumed by Ardhuin & Jenkins (2006) are different from the present study. Reconciliation of these findings at different scales is anticipated to yield new insights into air–sea interaction behaviour.

The data also provide understanding of the production of turbulent kinetic energy (TKE) in the upper ocean. Craig & Banner (1994) developed a boundary layer model for the upper ocean that incorporated both shear production of turbulence as well as injection of TKE from the wave field. These present data yield estimates of the TKE sourced from the wave field. From figure 15 (excluding the two data points showing high attenuation rates as discussed previously), the best fit is $\beta_{attn} = 2.62(ak)^{-1.43\pm0.21}$ (uncertainty, again, determined at 90 % confidence) which yields the expression:

$$S_{attn} = -1.31\sqrt{g}a^{0.57\pm0.21}k^{0.07\pm0.21}\rho_a u_*^{a^2} \tag{3.5}$$

with a correlation coefficient of 0.93 and where the ordering of the errors in the exponents must be correlated to maintain non-dimensionality. Craig & Banner (1994) report an expression equivalent to

$$S_{attn} = -100\rho_w u_*^{w^3} \sim S_{attn} = -3.5u_*^a\rho_a u_*^{a^2}. \tag{3.6}$$

Assuming equal air-sided and aqueous total stress and representative values for these present experiments of $u_*^a = 0.3$ m s^{-1}, $a = 0.015$ m and $k = 15$ m^{-1}, yields coefficients for S_{attn} of -0.45 and -1.05 in (3.5) and (3.6), respectively, thus reconciling the two expressions (equations (3.5) and (3.6)) almost within a factor of two.

Obtaining directly comparable values from the studies of Cheung & Street (1988) and Thais & Magnaudet (1996) was difficult. Using the data presented in figure 12 of

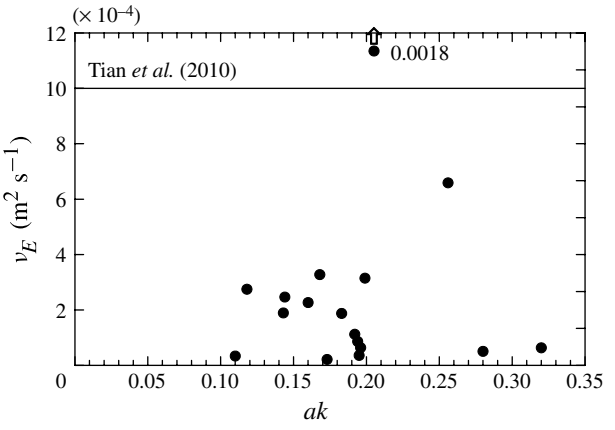

FIGURE 16. Eddy viscosity during active breaking as defined in (3.8).

Cheung & Street (1988), we attempted to obtain S_{turb} via

$$S_{turb} = \int_{-\lambda/2}^{0} \rho \overline{\tilde{u}\tilde{w}} \frac{\partial \overline{U}_w}{\partial z} \, \mathrm{d}z \tag{3.7}$$

where the tilde overbars indicate wave-induced water-side velocities and $\overline{U}_w$ indicates the mean horizontal water current. Cheung & Street (1988) show that this quantity declines monotonically with depth. Computing the integral of (3.7) at wind speeds of 4.1 and 6.2 m s^{-1} using an appropriate extrapolation of their data up to the mean water level yielded very large values of wave attenuation that could not be reconciled with this or any other investigation.

Re-examination of the findings of Cheung & Street (1988) and Thais & Magnaudet (1996) would be appropriate in light of the present study. Peirson *et al.* (2003) observed very strong rates of wave attenuation in the presence of opposing wind. Based on these present results, turbulent attenuation rates acting in concert with form drag of an opposing wind action on the wave would be anticipated to yield wave attenuation rates comparable with those observed by Peirson *et al.* (2003).

3.3.2. *Eddy viscosity approaches*

Tian *et al.* (2010) recently found that an eddy viscosity $\nu_E = 10^{-3}$ m^2 s^{-1} provided remarkable collapse to systematic measurements of wave breaking energy loss over carefully measured swept distances of wave breaking. For these present experiments, the eddy viscosity is defined as

$$\nu_E = \frac{S_{attn}}{4k^2 p_b E} \tag{3.8}$$

with p_b is the probability of observed breaking at a fixed point (table 1, column E). The equivalent eddy viscosities have been computed for the present measurements and are summarized in figure 16. As shown these do not yield a systematic collapse of the assembled measurements and the computed eddy viscosity values are approximately a factor of five smaller than values found by Tian *et al.* (2010).

It is noted that Drazen & Melville (2009) also computed eddy viscosities which collapse systematically as a function of breaking durations and span the range 10^{-4}

to 8×10^{-3} m^2 s^{-1}. We believe that while eddy viscosity concepts are attractive due to their simplicity, such approaches are unlikely to yield robust representations of highly non-stationary processes such as breaking.

3.3.3. *Duncan (1981) breaker model*

The present measurements permit examination of a key quantity in models of wind-forced development of sea state: the dissipation of wave energy due to breaking encapsulated in (1.12). In terms of the observations available here, we are converting the mean flux S_{attn} to a process that is localized at a point of breaking. In general, measuring localized breaking is a difficult process (Jessup & Phadnis 2005; Melville & Matusov 2002). During this present study, it was only possible to undertake point observations of breaking and define these as a probability of breaking of the dominant observable waves at a point.

A probability of observed breaking at a fixed point p_b (table 1, column E) implies a mean duration between breaking events T_b. Over the time duration T_b, the approximate mean length of wave surface that has propagated past the fixed point (ignoring surface dilation effects) is (Peirson & Banner 2001)

$$(c + u_{drift})T_b = \frac{2\pi(c + u_{drift})}{\omega p_b}. \tag{3.9}$$

Transforming the mean energy flux to energy dissipation per unit length of the breaking front:

$$\varepsilon_L = -\frac{2\pi S_{attn}\left(c + u_{drift}\right)}{\omega p_b}. \tag{3.10}$$

Equating (1.12) and (3.10), yields an expression for the breaking strength b:

$$b = -\frac{2\pi S_{attn}}{\rho_w\left(c + u_{drift}\right)^3 p_b} \tag{3.11}$$

where it has been assumed that the breaker speed is the same as the effective speed of waves at the spectral peak.

The b values computed are shown in figure 17 expressed as a function of wave steepness ak following the approach of Drazen *et al.* (2008). In figure 17, it can be observed that the present measurements sit appropriately between the determinations of Banner & Peirson (2007) and Drazen *et al.* (2008). This is a remarkable result which indicates overall robustness and closure to the present analysis. The curve fit recently developed by Romero, Melville & Kleiss (2012) is also shown in this figure.

As noted in the introduction, there is a growing body of evidence that the breaker speed c_{break} is less than the linear value of c by some 10 to 20 %. For present analysis, we have used the intrinsic wave speed c to match the analysis of Drazen *et al.* (2008) as closely as possible. Unfortunately, there was insufficient time to measure breaker speeds in detail. However, we note that any decrease in the breaker speeds below the intrinsic speed will cause the determined b values to sit correspondingly higher in figure 17.

The differences between the sets of measurements shown in figure 17 should be emphasized. The experiments of Banner & Peirson (2007) and Drazen *et al.* (2008) were conducted in the absence of wind when the only turbulence present was the turbulence generated by breaking events themselves. In contrast, the present investigations incorporate breaking events associated with waves propagating through turbulent water in which wind-induced shear is a strong feature.

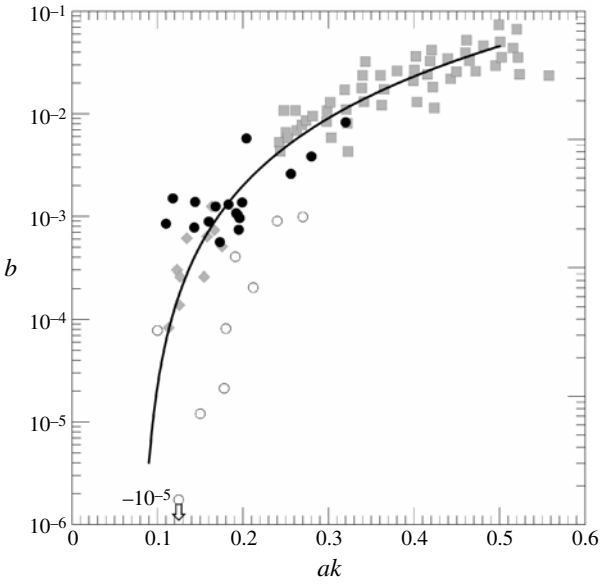

FIGURE 17. Breaking strength b expressed as a function of steepness ak. Data obtained from the present study is shown as solid circles, grey diamonds are data from Banner & Peirson (2007) and grey squares are data from Drazen *et al.* (2008). The equivalent non-breaking normalized dissipation rates are shown as hollow circles. The solid line is the fit $b = 0.4\,(ak - 0.08)^{5/2}$ from Romero *et al.* (2012).

Given the similarity in normalized attenuation rates between breaking and non-breaking waves shown in figure 15, does this mean that the Phillips representation is inappropriate and that (1.12) is merely a restatement of a dissipation form of (1.8)? To answer this question, we have added to figure 17 the b values characteristic of the non-breaking waves if their subsurface dissipation rates were attributed to a line source coinciding with the wave crests. As shown, these values are approximately a factor of 10 smaller than the breaking data cluster. This shows that:

(i) if wave attenuation is expressed in terms of wave parameters alone, the attenuation rates are approximately an order of magnitude higher in the presence of breaking;

(ii) these high attenuation rates are generated to match the higher wind-induced stresses induced by the breaking process itself (Banner 1990; Makin *et al.* 2007); and

(iii) if a partition between the wave attenuation contributions of localized surface breaking and spatially distributed wave–turbulent interactions is to be developed, the present results show that the surface breaking is the dominant contributor to the total attenuation of the wind-forced wave field.

4. Conclusions and recommendations

This present study has compared the input of energy by the wind to the waves with the observed growth response of the waves themselves. Achieving this goal has involved a suite of microphysical investigation techniques. The agreement of measured tangential stresses in the water and air immediately adjacent to the interface show consistency across a range of wave scales and in different experimental facilities.

The measured levels of viscous stress are approximately 50 % of those measured by Banner & Peirson (1998). This difference may reflect the higher levels of wave development for the waves investigated during this present study in contrast with Banner & Peirson (1998) who investigated the tangential stress during the initial phases of wave development at short fetch. Nonetheless, both studies show that substantial levels of viscous stress persist at moderate wind speeds.

The comparison between the tangential stresses measured in the air with corresponding form drag measurements show considerable consistency but it has highlighted some significant issues in relation to the measurement of fluctuating pressures above freely propagating waves. The extrapolations of form drag to a freely moving surface can result in a substantial overestimation of the form drag values. This overestimation occurs because of a significant change in the vertical gradient of $\overline{p\partial\eta/\partial x}$ that occurs at a normalized distance $k\xi = 0.5$ above the surface. Presumably this observed behaviour is related to air flow separation above the wave forms. The measurement of static pressure in an air flow above freely propagating waves requires specialist instruments that are subject to ambient pressure effects, including noise. The Deardorff (1967) equations have been extended to a wave-follower frame of reference. By measuring the total stress and fluctuating velocities in close proximity to the surface, the quantity $\overline{p\partial\eta/\partial x}$ can be obtained indirectly but with comparable accuracy to that of direct measurement. Such an approach may provide a more robust basis for measurements of wind input to waves under field conditions.

The normalized wind input values of the present study show good collapse as a function of wave steepness consistent with but at significantly higher levels than those obtained by Peirson & Garcia (2008) at moderate steepness.

The sheltering coefficients in the form of Jeffreys (1925) which have been derived from the present data are consistent in level with values previously obtained by Donelan & Pierson (1987), Donelan (1999) and Donelan *et al.* (2006). However, this normalization exhibits significant scatter within the assembled data. The normalized wind input does not show a good degree of collapse as a function of wave age. The instrumentation used to measure much of the data during this study should be sufficiently robust to capture the wave age dependency in the laboratory and, possibly, in the field.

For non-breaking waves, there is a significant misclose in the radiative transfer equation if wave–turbulence interactions are not included. These results support the conclusions of Cheung & Street (1988) of a momentum flux from the wave field to the aqueous layers below. Although not measured directly, energy budget estimates indicate a systematic wave–turbulence coupling as a function of wave steepness and at significantly higher levels than found theoretically by Teixeira & Belcher (2002) and Ardhuin & Jenkins (2006). Direct measurements of the turbulence in the water side are recommended to quantify these interactions.

The comparison of the wave energy budgets of the non-breaking and breaking cases shows that the normalized wave attenuation losses collapsed as a function of steepness ak except in a few specific and explicable cases. This finding indicates that in wind-forced wave fields containing regular breaking waves, the breaking events represent the augmentation necessary to maintain a balance between the wind input, turbulent attenuation and the development of the wave field. The energy loss rates due to breaking obtained during this present study are remarkably consistent with the values determined by Banner & Peirson (2007) and Drazen *et al.* (2008) for breaking waves when expressed as a function of mean wave steepness. Finally, a quantitative assessment is made of the finding by Tian *et al.* (2010) that the breaking process

can be represented by a constant eddy viscosity. Eddy viscosities computed from the data do not collapse systematically nor compare favourably with the Tian *et al.* (2010) value.

Acknowledgements

Funding by the Australian Research Council for W.L.P. under Discovery Project 0452505 for this project and ongoing support under Discovery Projects 1095722 and 0985602 is gratefully acknowledged. The hospitality of the Institut de Recherche sur les Phénomènes Hors Équilibre, Marseille for W.L.P. during this study is appreciated. During the revision and final preparation of this paper the senior author (L.G.) was supported at Scripps Institution of Oceanography by grants from the Office of Naval Research (Physical Oceanography) and the National Science Foundation (Ocean Sciences) to W.K. Melville. Conducting such difficult laboratory investigations would be impossible without the skill and diligence of technical support staff. The authors thank Messrs B. Zucchini and A. Laurence for their helpful technical assistance during the IRPHE experimental investigations. The late Mr J. Hart made an enormous contribution to the manufacture and installation of the specialist precise equipment used at the Water Research Laboratory. Mrs W. Thomason-Harper assisted with the typesetting of the equations and Mrs A. Blacka drafted the technical diagrams. The willing assistance of the support staff at both laboratories is gratefully appreciated.

Appendix. Momentum fluxes written in the frame of the wave follower

Transforming from the Cartesian frame $x_i^* = (x, y, z, t)$ to the curvilinear wave-following frame $x_i = (x, y, \xi, t)$, with $\xi = z - \eta$ (figure 18), requires the following identities:

$$(x, y, z, t) \to (x, y, \xi, t) : \frac{\partial}{\partial x_i^*} = \frac{\partial}{\partial x_i} - \frac{\partial \eta}{\partial x_i}\frac{\partial}{\partial \xi} \tag{A 1a}$$

$$\frac{\partial}{\partial t} = \frac{\partial}{\partial x}\frac{\partial x}{\partial t} + \frac{\partial}{\partial y}\frac{\partial y}{\partial t} + \frac{\partial}{\partial \xi}\frac{\partial \xi}{\partial t} + \frac{\partial}{\partial t}\frac{\partial t}{\partial t} = -\frac{\partial}{\partial \xi}\frac{\partial \eta}{\partial t} + \frac{\partial}{\partial t}. \tag{A 1b}$$

In the curvilinear frame, the Navier–Stokes equations become

$$\begin{aligned}\frac{\partial u_i}{\partial t} + \frac{\partial u_i u_j}{\partial x_j} + \frac{1}{\rho}\frac{\partial p}{\partial x_i} - \nu\frac{\partial^2 u_i}{\partial x_j^2} &= \frac{\partial \eta}{\partial t}\frac{\partial u_i}{\partial \xi} + \frac{\partial \eta}{\partial x_j}\frac{\partial u_i u_j}{\partial \xi} + \frac{1}{\rho}\frac{\partial \eta}{\partial x_i}\frac{\partial p}{\partial \xi} \\ &+ \nu\left(\frac{\partial \eta}{\partial x_j}\right)^2\frac{\partial^2 u_i}{\partial \xi^2} - \nu\frac{\partial^2 \eta}{\partial x_j^2}\frac{\partial u_i}{\partial \xi} - 2\nu\frac{\partial \eta}{\partial x_j}\frac{\partial^2 u_i}{\partial \xi \partial x_j} + \nu\frac{\partial^2 \eta}{\partial x_i^2}\frac{\partial u_i}{\partial \xi}.\end{aligned} \tag{A 2}$$

A.1. *x-component*

Equations (A 2) projected along the unit normal in the x-direction $\boldsymbol{x}$ become

$$\begin{aligned}&\frac{\partial u}{\partial t} + \frac{\partial}{\partial x}\left(u^2 + \frac{p}{\rho} - \nu\frac{\partial u}{\partial x}\right) + \frac{\partial}{\partial y}\left(uv - \nu\frac{\partial u}{\partial y}\right) + \frac{\partial}{\partial \xi}\left(uw - \nu\frac{\partial u}{\partial \xi}\right) \\ &= \frac{\partial \eta}{\partial t}\frac{\partial u}{\partial \xi} + \frac{\partial \eta}{\partial x}\frac{\partial}{\partial \xi}\left(u^2 + \frac{p}{\rho} + \nu\frac{\partial \eta}{\partial x}\frac{\partial u}{\partial \xi} - 2\nu\frac{\partial u}{\partial x}\right) \\ &+ \frac{\partial \eta}{\partial y}\frac{\partial}{\partial \xi}\left(uv + \nu\frac{\partial \eta}{\partial y}\frac{\partial u}{\partial \xi} - 2\nu\frac{\partial u}{\partial y}\right) - \nu\left(\frac{\partial^2 \eta}{\partial x^2} + \frac{\partial^2 \eta}{\partial y^2}\right)\frac{\partial u}{\partial \xi}.\end{aligned} \tag{A 3}$$

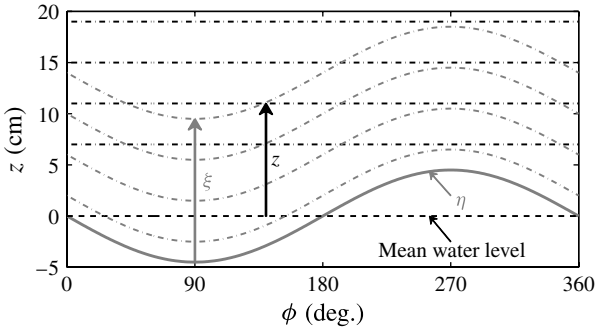

FIGURE 18. Cartesian and curvilinear wave-following frames.

Integrating between $\xi = 0$ and $\xi = h$, we have

$$\int_0^h \frac{\partial u}{\partial t}\,\mathrm{d}\xi + \int_0^h \frac{\partial}{\partial x}\left(u^2 + \frac{p}{\rho} - \nu\frac{\partial u}{\partial x}\right)\mathrm{d}\xi + \int_0^h \frac{\partial}{\partial y}\left(uv - \nu\frac{\partial u}{\partial y}\right)\mathrm{d}\xi + \int_0^h \frac{\partial}{\partial \xi}\left(uw - \nu\frac{\partial u}{\partial \xi}\right)\mathrm{d}\xi$$
$$= \int_0^h \frac{\partial \eta}{\partial t}\frac{\partial u}{\partial \xi}\,\mathrm{d}\xi + \int_0^h \frac{\partial \eta}{\partial x}\frac{\partial}{\partial \xi}\left(u^2 + \frac{p}{\rho} + \nu\frac{\partial \eta}{\partial x}\frac{\partial u}{\partial \xi} - 2\nu\frac{\partial u}{\partial x}\right)\mathrm{d}\xi + \int_0^h \frac{\partial \eta}{\partial y}\frac{\partial}{\partial \xi}\left(uv + \nu\frac{\partial \eta}{\partial y}\frac{\partial u}{\partial \xi} - 2\nu\frac{\partial u}{\partial y}\right)\mathrm{d}\xi - \nu\int_0^h \left(\frac{\partial^2 \eta}{\partial x^2} + \frac{\partial^2 \eta}{\partial y^2}\right)\frac{\partial u}{\partial \xi}\,\mathrm{d}\xi \quad (A\,4)$$

which can be simplified as

$$\frac{\partial}{\partial t}\int_0^h u\,\mathrm{d}\xi + \int_0^h \frac{\partial}{\partial x}\left(u^2 + \frac{p}{\rho} - \nu\frac{\partial u}{\partial x}\right)\mathrm{d}\xi + \int_0^h \frac{\partial}{\partial y}\left(uv - \nu\frac{\partial u}{\partial y}\right)\mathrm{d}\xi + \left[uw - \nu\frac{\partial u}{\partial \xi}\right]_0^h$$
$$= \frac{\partial \eta}{\partial t}[u]_0^h + \frac{\partial \eta}{\partial x}\left[u^2 + \frac{p}{\rho} + \nu\frac{\partial \eta}{\partial x}\frac{\partial u}{\partial \xi} - 2\nu\frac{\partial u}{\partial x}\right]_0^h + \frac{\partial \eta}{\partial y}\left[uv + \nu\frac{\partial \eta}{\partial y}\frac{\partial u}{\partial \xi} - 2\nu\frac{\partial u}{\partial y}\right]_0^h$$
$$- \nu\left(\frac{\partial^2 \eta}{\partial x^2} + \frac{\partial^2 \eta}{\partial y^2}\right)[u]_0^h. \quad (A\,5)$$

Using the kinematic condition at the surface $w_0 = \partial\eta/\partial t + u_0(\partial\eta/\partial x) + v_0(\partial\eta/\partial y)$, equation (A 5) can be simplified as

$$\frac{\partial}{\partial t}\int_0^h u\,\mathrm{d}\xi + \int_0^h \frac{\partial}{\partial x}\left(u^2 + \frac{p}{\rho} - \nu\frac{\partial u}{\partial x}\right)\mathrm{d}\xi + \int_0^h \frac{\partial}{\partial y}\left(uv - \nu\frac{\partial u}{\partial y}\right)\mathrm{d}\xi + [uw]^h - \nu\left[\frac{\partial u}{\partial \xi}\right]_0^h$$
$$= \frac{\partial \eta}{\partial t}[u]^h + \frac{\partial \eta}{\partial x}\left[u^2\right]^h + \frac{\partial \eta}{\partial x}\left[\frac{p}{\rho} + \nu\frac{\partial \eta}{\partial x}\frac{\partial u}{\partial \xi} - 2\nu\frac{\partial u}{\partial x}\right]_0^h + \frac{\partial \eta}{\partial y}[uv]^h$$
$$+ \nu\frac{\partial \eta}{\partial y}\left[\frac{\partial \eta}{\partial y}\frac{\partial u}{\partial \xi} - 2\nu\frac{\partial u}{\partial y}\right]_0^h - \nu\left(\frac{\partial^2 \eta}{\partial x^2} + \frac{\partial^2 \eta}{\partial y^2}\right)[u]_0^h. \quad (A\,6)$$

Applying the time-averaging operator to equation (A 6) yields

$$\begin{aligned}
&\overline{\frac{\partial}{\partial t}\int_0^h u\,\mathrm{d}\xi} + \overline{\int_0^h \frac{\partial}{\partial x}\left(u^2 + \frac{p}{\rho} - \nu\frac{\partial u}{\partial x}\right)\mathrm{d}\xi} + \overline{\int_0^h \frac{\partial}{\partial y}\left(uv - \nu\frac{\partial u}{\partial y}\right)\mathrm{d}\xi} \\
&\quad + \overline{uw}|_h - \nu\overline{\left[\frac{\partial u}{\partial \xi}\right]_0^h} \\
&= \overline{u_h\frac{\partial \eta}{\partial t}} + \overline{u_h^2\frac{\partial \eta}{\partial x}} + \overline{\frac{\partial \eta}{\partial x}\left[\frac{p}{\rho} + \nu\frac{\partial \eta}{\partial x}\frac{\partial u}{\partial \xi} - 2\nu\frac{\partial u}{\partial x}\right]_0^h} + \overline{(uv)_h\frac{\partial \eta}{\partial y}} + \nu\overline{\frac{\partial \eta}{\partial y}\left[\frac{\partial \eta}{\partial y}\frac{\partial u}{\partial \xi} - 2\frac{\partial u}{\partial y}\right]_0^h} \\
&\quad - \nu\overline{\left(\frac{\partial^2 \eta}{\partial x^2} + \frac{\partial^2 \eta}{\partial y^2}\right)[u]_0^h}.
\end{aligned} \tag{A 7}$$

Assuming steady flow and mean integrated horizontal gradients much smaller than their vertical counterparts:

$$\left.\begin{aligned}
&\overline{\int_0^h \frac{\partial}{\partial x}\ldots\,\mathrm{d}\xi} \ll \overline{\int_0^h \frac{\partial}{\partial \xi}\ldots\,\mathrm{d}\xi};\quad \overline{\int_0^h \frac{\partial}{\partial y}\ldots\,\mathrm{d}\xi} \ll \overline{\int_0^h \frac{\partial}{\partial \xi}\ldots\,\mathrm{d}\xi};\quad \text{and} \\
&\overline{\frac{\partial}{\partial t}\int_0^h u\,\mathrm{d}\xi} = 0
\end{aligned}\right\} \tag{A 8}$$

one obtains

$$\begin{aligned}
&-\overline{uw}|_h + \overline{u_h\frac{\partial \eta}{\partial t}} + \overline{u_h^2\frac{\partial \eta}{\partial x}} + \overline{(uv)_h\frac{\partial \eta}{\partial y}} + \frac{1}{\rho}\overline{p_h\frac{\partial \eta}{\partial x}} \\
&\quad + \nu\overline{\frac{\partial u}{\partial \xi}\bigg|_h} + \nu\overline{\left(\frac{\partial \eta}{\partial x}\right)^2\frac{\partial u}{\partial \xi}\bigg|_h} - 2\nu\left(\overline{\frac{\partial \eta}{\partial x}\frac{\partial u}{\partial x}\bigg|_h} + \overline{\frac{\partial \eta}{\partial y}\frac{\partial u}{\partial y}\bigg|_h}\right) - \nu\overline{\left(\frac{\partial^2 \eta}{\partial x^2} + \frac{\partial^2 \eta}{\partial y^2}\right)u_h} \\
&= \overline{\frac{1}{\rho}p_0\frac{\partial \eta}{\partial x}} + \nu\overline{\frac{\partial u}{\partial \xi}\bigg|_0} + \nu\overline{\left(\frac{\partial \eta}{\partial x}\right)^2\frac{\partial u}{\partial \xi}\bigg|_0} - 2\nu\left(\overline{\frac{\partial \eta}{\partial x}\frac{\partial u}{\partial x}\bigg|_0} + \overline{\frac{\partial \eta}{\partial y}\frac{\partial u}{\partial y}\bigg|_0}\right) \\
&\quad - \nu\overline{\underbrace{\left(\frac{\partial^2 \eta}{\partial x^2} + \frac{\partial^2 \eta}{\partial y^2}\right)}_{\nabla^2\eta}u_0}
\end{aligned} \tag{A 9}$$

yielding

$$\begin{aligned}
{}_x\tau^h &= \text{Total stress} \\
&= {}_x\tau_a^h + {}_x\tau_p^h + {}_x\tau_\nu^h = {}_x\tau_p^0 + {}_x\tau_\nu^0 && \text{(A 10}a\text{)} \\
{}_x\tau_a^h &= \text{Terms due to wave-follower motion} \\
&= -\rho\,\overline{uw}|_h + \rho\overline{u_h\frac{\partial \eta}{\partial t}} + \rho\overline{u_h^2\frac{\partial \eta}{\partial x}} + \rho\overline{(uv)_h\frac{\partial \eta}{\partial y}} && \text{(A 10}b\text{)} \\
{}_x\tau_p^h &= \text{Pressure–slope correlations at height } h \\
&= \overline{p_h\frac{\partial \eta}{\partial x}} && \text{(A 10}c\text{)}
\end{aligned}$$

$$
\begin{aligned}
{}_x\tau_v^h &= \text{Viscous stress at height } h \\
&= \mu\,\overline{\left.\frac{\partial u}{\partial \xi}\right|_h} + \mu\,\overline{\left.\left(\frac{\partial \eta}{\partial x}\right)^2 \frac{\partial u}{\partial \xi}\right|_h} - 2\mu\left(\overline{\left.\frac{\partial \eta}{\partial x}\frac{\partial u}{\partial x}\right|_h} + \overline{\left.\frac{\partial \eta}{\partial y}\frac{\partial u}{\partial y}\right|_h}\right) - \mu\overline{\Delta\eta u_h} \quad \text{(A 10}d\text{)} \\
{}_x\tau_p^0 &= \text{Form drag} \\
&= \overline{p_0\frac{\partial \eta}{\partial x}} \quad \text{(A 10}e\text{)} \\
{}_x\tau_v^0 &= \text{Tangential stress} \\
&= \mu\,\overline{\left.\frac{\partial u}{\partial \xi}\right|_0} + \mu\,\overline{\left.\left(\frac{\partial \eta}{\partial x}\right)^2 \frac{\partial u}{\partial \xi}\right|_0} - 2\mu\left(\overline{\left.\frac{\partial \eta}{\partial x}\frac{\partial u}{\partial x}\right|_0} + \overline{\left.\frac{\partial \eta}{\partial y}\frac{\partial u}{\partial y}\right|_0}\right) - \mu\overline{\Delta\eta u_0}. \quad \text{(A 10}f\text{)}
\end{aligned}
$$

Decomposing the velocity and pressure components into mean (indicated by overbars) and fluctuating (indicated by primes) components, equations (A 10*b*)–(A 10*f*) become

$$
\begin{aligned}
{}_x\tau_v^h &= \mu\left.\frac{\partial \overline{u}}{\partial \xi}\right|_h + \mu\,\overline{\left.\left(\frac{\partial \eta}{\partial x}\right)^2 \frac{\partial u'}{\partial \xi}\right|_h} + \mu\,\overline{\left.\left(\frac{\partial \eta}{\partial x}\right)^2\right|}\left.\frac{\partial \overline{u}}{\partial \xi}\right|_h \\
&\quad - 2\mu\left(\overline{\left.\frac{\partial \eta}{\partial x}\frac{\partial u'}{\partial x}\right|_h} + \overline{\left.\frac{\partial \eta}{\partial y}\frac{\partial u'}{\partial y}\right|_h}\right) - \mu\overline{\Delta\eta u'_h} - \mu\overline{\Delta\eta}\,\overline{u}_h \quad \text{(A 11}a\text{)} \\
{}_x\tau_a^h &= -\rho\,\overline{\left.u'w'\right|_h} + \rho\overline{u'_h\frac{\partial \eta}{\partial t}} + \rho\overline{u'^2_h}\frac{\partial \overline{\eta}}{\partial x} + 2\rho\overline{u}_h\overline{u'_h\frac{\partial \eta}{\partial x}} \\
&\quad + \rho\overline{(u'v')_h\frac{\partial \eta}{\partial y}} + \rho\overline{u}\,\overline{v'\frac{\partial \eta}{\partial y}} + \rho\overline{v}\overline{u'\frac{\partial \eta}{\partial y}} \quad \text{(A 11}b\text{)} \\
{}_x\tau_p^h &= \overline{p'_h\frac{\partial \eta}{\partial x}} \quad \text{(A 11}c\text{)} \\
{}_x\tau_v^0 &= \mu\left.\frac{\partial \overline{u}}{\partial \xi}\right|_0 + \mu\,\overline{\left.\left(\frac{\partial \eta}{\partial x}\right)^2 \frac{\partial u'}{\partial \xi}\right|_0} + \mu\,\overline{\left.\left(\frac{\partial \eta}{\partial x}\right)^2\right|}\left.\frac{\partial \overline{u}}{\partial \xi}\right|_0 \\
&\quad - 2\mu\left(\overline{\left.\frac{\partial \eta}{\partial x}\frac{\partial u'}{\partial x}\right|_0} + \overline{\left.\frac{\partial \eta}{\partial y}\frac{\partial u'}{\partial y}\right|_0}\right) - \mu\overline{\Delta\eta u'_0} - \mu\overline{\Delta\eta}\,\overline{u}_0 \quad \text{(A 11}d\text{)} \\
{}_x\tau_p^0 &= \overline{p'_0\frac{\partial \eta}{\partial x}}. \quad \text{(A 11}e\text{)}
\end{aligned}
$$

Further decomposing the fluctuations components into wave-induced (tilde overbars) and turbulent (double primes) components, equations (A 11*a*)–(A 11*e*) become

$$
\begin{aligned}
{}_x\tau_v^h &= \mu\left.\frac{\partial \overline{u}}{\partial \xi}\right|_h + \mu\,\overline{\left.\left(\frac{\partial \eta}{\partial x}\right)^2 \frac{\partial \tilde{u}}{\partial \xi}\right|_h} + \mu\,\overline{\left.\left(\frac{\partial \eta}{\partial x}\right)^2 \frac{\partial u''}{\partial \xi}\right|_h} + \mu\,\overline{\left.\left(\frac{\partial \eta}{\partial x}\right)^2\right|}\left.\frac{\partial \overline{u}}{\partial \xi}\right|_h \\
&\quad - 2\mu\left(\overline{\left.\frac{\partial \eta}{\partial x}\frac{\partial \tilde{u}}{\partial x}\right|_h} + \overline{\left.\frac{\partial \eta}{\partial y}\frac{\partial \tilde{u}}{\partial y}\right|_h}\right) - 2\mu\left(\overline{\left.\frac{\partial \eta}{\partial x}\frac{\partial u''}{\partial x}\right|_h} + \overline{\left.\frac{\partial \eta}{\partial y}\frac{\partial u''}{\partial y}\right|_h}\right) \\
&\quad - \mu\overline{\Delta\eta\tilde{u}_h} - \mu\overline{\Delta\eta u''_h} - \mu\overline{\Delta\eta}\,\overline{u}_h \quad \text{(A 12}a\text{)}
\end{aligned}
$$

$$
\begin{aligned}
{}_x\tau_a^h &= -\rho\overline{\tilde{u}\tilde{w}}\Big|_h - \rho\overline{u''w''}\Big|_h + \rho\overline{\tilde{u}_h\frac{\partial\eta}{\partial t}} + \rho\overline{\tilde{u}_h^2\frac{\partial\eta}{\partial x}} + \rho\overline{u_h''^2\frac{\partial\eta}{\partial x}} + 2\rho\overline{u}_h\overline{\tilde{u}_h\frac{\partial\eta}{\partial x}} \\
&\quad + \rho\overline{(\tilde{u}\tilde{v})_h\frac{\partial\eta}{\partial y}} + \rho\overline{(u''v'')_h\frac{\partial\eta}{\partial y}} + \rho\overline{u}\overline{\tilde{v}\frac{\partial\eta}{\partial y}} + \rho\overline{v}\overline{\tilde{u}\frac{\partial\eta}{\partial y}} \qquad \text{(A 12}b\text{)} \\
{}_x\tau_p^h &= \overline{\tilde{p}_h\frac{\partial\eta}{\partial x}} \qquad \text{(A 12}c\text{)} \\
{}_x\tau_v^0 &= \mu\frac{\partial\overline{u}}{\partial\xi}\Big|_0 + \mu\overline{\left(\frac{\partial\eta}{\partial x}\right)^2\frac{\partial\tilde{u}}{\partial\xi}}\Big|_0 + \mu\overline{\left(\frac{\partial\eta}{\partial x}\right)^2\frac{\partial u''}{\partial\xi}}\Big|_0 + \mu\overline{\left(\frac{\partial\eta}{\partial x}\right)^2}\frac{\partial\overline{u}}{\partial\xi}\Big|_0 \\
&\quad - 2\mu\left(\overline{\frac{\partial\eta}{\partial x}\frac{\partial\tilde{u}}{\partial x}}\Big|_0 + \overline{\frac{\partial\eta}{\partial y}\frac{\partial\tilde{u}}{\partial y}}\Big|_0\right) - 2\mu\left(\overline{\frac{\partial\eta}{\partial x}\frac{\partial u''}{\partial x}}\Big|_0 + \overline{\frac{\partial\eta}{\partial y}\frac{\partial u''}{\partial y}}\Big|_0\right) \\
&\quad - \mu\overline{\Delta\eta\tilde{u}_0} - \mu\overline{\Delta\eta u_0''} - \mu\overline{\Delta\eta}\overline{u}_0 \qquad \text{(A 12}d\text{)} \\
{}_x\tau_p^0 &= \overline{\tilde{p}_0\frac{\partial\eta}{\partial x}}. \qquad \text{(A 12}e\text{)}
\end{aligned}
$$

A.2. *y-component*

We now write the momentum flux in the transverse direction ($\boldsymbol{y}$). Equations (A 2) projected along $\boldsymbol{y}$ become

$$
\begin{aligned}
&\frac{\partial v}{\partial t} + \frac{\partial}{\partial x}\left(uv - \nu\frac{\partial v}{\partial x}\right) + \frac{\partial}{\partial y}\left(v^2 + \frac{p}{\rho} - \nu\frac{\partial v}{\partial y}\right) + \frac{\partial}{\partial\xi}\left(vw - \nu\frac{\partial v}{\partial\xi}\right) \\
&\quad = \frac{\partial\eta}{\partial t}\frac{\partial v}{\partial\xi} + \frac{\partial\eta}{\partial x}\frac{\partial}{\partial\xi}\left(uv + \nu\frac{\partial\eta}{\partial x}\frac{\partial v}{\partial\xi} - 2\nu\frac{\partial v}{\partial x}\right) + \frac{\partial\eta}{\partial y}\frac{\partial}{\partial\xi}\left(v^2 + \frac{p}{\rho} + \nu\frac{\partial\eta}{\partial y}\frac{\partial v}{\partial\xi} - 2\nu\frac{\partial v}{\partial y}\right) \\
&\qquad - \nu\left(\frac{\partial^2\eta}{\partial x^2} + \frac{\partial^2\eta}{\partial y^2}\right)\frac{\partial v}{\partial\xi}. \qquad \text{(A 13)}
\end{aligned}
$$

Integrating between $\xi = 0$ and $\xi = h$:

$$
\begin{aligned}
&\int_0^h \frac{\partial v}{\partial t}\,\mathrm{d}\xi + \int_0^h \frac{\partial}{\partial x}\left(uv - \nu\frac{\partial v}{\partial x}\right)\mathrm{d}\xi + \int_0^h \frac{\partial}{\partial y}\left(v^2 + \frac{p}{\rho} - \nu\frac{\partial v}{\partial y}\right)\mathrm{d}\xi \\
&\qquad + \int_0^h \frac{\partial}{\partial\xi}\left(vw - \nu\frac{\partial v}{\partial\xi}\right)\mathrm{d}\xi \\
&\quad = \int_0^h \frac{\partial\eta}{\partial t}\frac{\partial v}{\partial\xi}\,\mathrm{d}\xi + \int_0^h \frac{\partial\eta}{\partial x}\frac{\partial}{\partial\xi}\left(uv + \nu\frac{\partial\eta}{\partial x}\frac{\partial v}{\partial\xi} - 2\nu\frac{\partial v}{\partial x}\right)\mathrm{d}\xi \\
&\qquad + \int_0^h \frac{\partial\eta}{\partial y}\frac{\partial}{\partial\xi}\left(v^2 + \frac{p}{\rho} + \nu\frac{\partial\eta}{\partial y}\frac{\partial v}{\partial\xi} - 2\nu\frac{\partial v}{\partial y}\right)\mathrm{d}\xi \\
&\qquad - \nu\int_0^h \left(\frac{\partial^2\eta}{\partial x^2} + \frac{\partial^2\eta}{\partial y^2}\right)\frac{\partial v}{\partial\xi}\,\mathrm{d}\xi \qquad \text{(A 14)}
\end{aligned}
$$

yielding

$$
{}_y\tau^h = {}_y\tau_v^h + {}_y\tau_a^h + {}_y\tau_p^h = {}_y\tau_v^h + {}_y\tau_p^h \qquad \text{(A 15}a\text{)}
$$

and

$$ {}_y\tau_v^h = \mu \left.\overline{\frac{\partial v}{\partial \xi}}\right|_h + \mu \left.\overline{\left(\frac{\partial \eta}{\partial x}\right)^2 \frac{\partial v}{\partial \xi}}\right|_h - 2\mu \left(\left.\overline{\frac{\partial \eta}{\partial x}\frac{\partial v}{\partial x}}\right|_h + \left.\overline{\frac{\partial \eta}{\partial y}\frac{\partial v}{\partial y}}\right|_h \right) - \mu\overline{\Delta\eta v_h} \quad \text{(A 15}b\text{)} $$

$$ {}_y\tau_a^h = -\rho\,\overline{vw}|_h + \rho v_h \overline{\frac{\partial \eta}{\partial t}} + \rho\overline{(uv)_h \frac{\partial \eta}{\partial x}} + \rho\overline{v_h^2 \frac{\partial \eta}{\partial y}} \quad \text{(A 15}c\text{)} $$

$$ {}_y\tau_p^h = \overline{p_h \frac{\partial \eta}{\partial y}} \quad \text{(A 15}d\text{)} $$

$$ {}_y\tau_v^0 = \mu \left.\overline{\frac{\partial v}{\partial \xi}}\right|_0 + \mu \left.\overline{\left(\frac{\partial \eta}{\partial x}\right)^2 \frac{\partial v}{\partial \xi}}\right|_0 - 2\mu \left(\left.\overline{\frac{\partial \eta}{\partial x}\frac{\partial v}{\partial x}}\right|_0 + \left.\overline{\frac{\partial \eta}{\partial y}\frac{\partial v}{\partial y}}\right|_0 \right) - \mu\overline{\Delta\eta v_0} \quad \text{(A 15}e\text{)} $$

$$ {}_y\tau_p^0 = \overline{p_0 \frac{\partial \eta}{\partial y}}. \quad \text{(A 15}f\text{)} $$

Decomposing the velocity and pressure components into mean (indicated by overbars) and fluctuating (indicated by primes) components, equations (A 15*b*)–(A 15*f*) become

$$ \begin{aligned} {}_y\tau_v^h = {} & \mu \left.\frac{\partial \overline{v}}{\partial \xi}\right|_h + \mu \left.\overline{\left(\frac{\partial \eta}{\partial x}\right)^2 \frac{\partial v'}{\partial \xi}}\right|_h + \mu \left.\overline{\left(\frac{\partial \eta}{\partial x}\right)^2} \frac{\partial \overline{v}}{\partial \xi}\right|_h \\ & - 2\mu \left(\left.\overline{\frac{\partial \eta}{\partial x}\frac{\partial v'}{\partial x}}\right|_h + \left.\overline{\frac{\partial \eta}{\partial y}\frac{\partial v'}{\partial y}}\right|_h \right) - \mu\overline{\Delta\eta v_h'} - \mu\overline{\Delta\eta}\,\overline{v}_h \end{aligned} \quad \text{(A 16}a\text{)} $$

$$ \begin{aligned} {}_y\tau_a^h = {} & -\rho\,\overline{v'w'}|_h + \rho\overline{v_h' \frac{\partial \eta}{\partial t}} + \rho\overline{v_h'^2 \frac{\partial \eta}{\partial y}} + 2\rho\overline{v}_h\overline{v_h' \frac{\partial \eta}{\partial y}} \\ & + \rho\overline{(u'v')_h \frac{\partial \eta}{\partial x}} + \rho\overline{u}_h\overline{v_h' \frac{\partial \eta}{\partial x}} + \rho\overline{v}_h\overline{u_h' \frac{\partial \eta}{\partial x}} \end{aligned} \quad \text{(A 16}b\text{)} $$

$$ {}_y\tau_p^h = \overline{p_h' \frac{\partial \eta}{\partial y}} \quad \text{(A 16}c\text{)} $$

$$ \begin{aligned} {}_y\tau_v^0 = {} & \mu \left.\frac{\partial \overline{v}}{\partial \xi}\right|_0 + \mu \left.\overline{\left(\frac{\partial \eta}{\partial x}\right)^2 \frac{\partial v'}{\partial \xi}}\right|_0 + \mu \left.\overline{\left(\frac{\partial \eta}{\partial x}\right)^2} \frac{\partial \overline{v}}{\partial \xi}\right|_0 \\ & - 2\mu \left(\left.\overline{\frac{\partial \eta}{\partial x}\frac{\partial v'}{\partial x}}\right|_0 + \left.\overline{\frac{\partial \eta}{\partial y}\frac{\partial v'}{\partial y}}\right|_0 \right) - \mu\overline{\Delta\eta v_0'} - \mu\overline{\Delta\eta}\,\overline{v}_0 \end{aligned} \quad \text{(A 16}d\text{)} $$

$$ {}_y\tau_p^0 = \overline{p_0' \frac{\partial \eta}{\partial y}}. \quad \text{(A 16}e\text{)} $$

Further decomposing the fluctuations components into wave-induced (tilde overbars) and turbulent (double primes) components, equations (A 16*a*)–(A 16*e*) become

$$ \begin{aligned} {}_y\tau_v^h = {} & \mu \left.\frac{\partial \overline{v}}{\partial \xi}\right|_h + \mu \left.\overline{\left(\frac{\partial \eta}{\partial x}\right)^2 \frac{\partial \tilde{v}}{\partial \xi}}\right|_h + \mu \left.\overline{\left(\frac{\partial \eta}{\partial x}\right)^2 \frac{\partial v''}{\partial \xi}}\right|_h + \mu \left.\overline{\left(\frac{\partial \eta}{\partial x}\right)^2} \frac{\partial \overline{v}}{\partial \xi}\right|_h \\ & - 2\mu \left(\left.\overline{\frac{\partial \eta}{\partial x}\frac{\partial \tilde{v}}{\partial x}}\right|_h + \left.\overline{\frac{\partial \eta}{\partial y}\frac{\partial \tilde{v}}{\partial y}}\right|_h \right) - 2\mu \left(\left.\overline{\frac{\partial \eta}{\partial x}\frac{\partial v''}{\partial x}}\right|_h + \left.\overline{\frac{\partial \eta}{\partial y}\frac{\partial v''}{\partial y}}\right|_h \right) \\ & - \mu\overline{\Delta\eta\tilde{v}_h} - \mu\overline{\Delta\eta v_h''} - \mu\overline{\Delta\eta}\,\overline{v}_h \end{aligned} \quad \text{(A 17}a\text{)} $$

$$
\begin{aligned}
{}_y\tau_a^h &= -\rho\,\overline{\tilde{v}\tilde{w}}\Big|_h - \rho\,\overline{v''w''}\big|_h + \rho\overline{\tilde{v}_h\frac{\partial\eta}{\partial t}} + \rho\overline{\tilde{v}_h^2\frac{\partial\eta}{\partial y}} + \rho\overline{v_h''^2\frac{\partial\eta}{\partial y}} + 2\rho\overline{v}_h\overline{\tilde{v}_h\frac{\partial\eta}{\partial y}} \\
&\quad + \rho\overline{(\tilde{u}\tilde{v})_h\frac{\partial\eta}{\partial x}} + \rho\overline{(u''v'')_h\frac{\partial\eta}{\partial x}} + \rho\overline{u}_h\overline{\tilde{v}_h\frac{\partial\eta}{\partial x}} + \rho\overline{v}_h\overline{\tilde{u}_h\frac{\partial\eta}{\partial x}} \qquad \text{(A 17}b\text{)} \\
{}_y\tau_p^h &= \overline{\tilde{p}_h\frac{\partial\eta}{\partial y}} \qquad \text{(A 17}c\text{)} \\
{}_y\tau_\nu^0 &= \mu\,\frac{\partial\overline{v}}{\partial\xi}\Big|_0 + \mu\,\overline{\left(\frac{\partial\eta}{\partial x}\right)^2\frac{\partial\tilde{v}}{\partial\xi}}\Big|_0 + \mu\,\overline{\left(\frac{\partial\eta}{\partial x}\right)^2\frac{\partial v''}{\partial\xi}}\Big|_0 + \mu\,\overline{\left(\frac{\partial\eta}{\partial x}\right)^2}\frac{\partial\overline{v}}{\partial\xi}\Big|_0 \\
&\quad - 2\mu\left(\overline{\frac{\partial\eta}{\partial x}\frac{\partial\tilde{v}}{\partial x}}\Big|_0 + \overline{\frac{\partial\eta}{\partial y}\frac{\partial\tilde{v}}{\partial y}}\Big|_0\right) - 2\mu\left(\overline{\frac{\partial\eta}{\partial x}\frac{\partial v''}{\partial x}}\Big|_0 + \overline{\frac{\partial\eta}{\partial y}\frac{\partial v''}{\partial y}}\Big|_0\right) \\
&\quad - \mu\overline{\Delta\eta\tilde{v}_0} - \mu\overline{\Delta\eta v_0''} - \mu\overline{\Delta\eta}\overline{v}_0 \qquad \text{(A 17}d\text{)} \\
{}_y\tau_p^0 &= \overline{\tilde{p}_0\frac{\partial\eta}{\partial y}}. \qquad \text{(A 17}e\text{)}
\end{aligned}
$$

The total momentum flux is a vector and the total stress becomes

$$\boldsymbol{\tau} = {}_x\tau\boldsymbol{x} + {}_y\tau\boldsymbol{y} \qquad \text{(A 18}a\text{)}$$

with

$${}_x\tau = {}_x\tau_p^0 + {}_x\tau_\nu^0 = {}_x\tau_a^h + {}_x\tau_p^h + {}_x\tau_\nu^h \qquad \text{(A 18}b\text{)}$$

and

$${}_y\tau = {}_y\tau_p^0 + {}_y\tau_\nu^0 = {}_y\tau_a^h + {}_y\tau_p^h + {}_y\tau_\nu^h. \qquad \text{(A 18}c\text{)}$$

If we now suppose the flow and waves are two-dimensional and the gradients of the turbulent quantities are small relative to the gradients of the wave-induced quantities, the transversal stress ${}_y\tau$ is null, and the total stress is only supported by ${}_x\tau$:

$$\tau = {}_x\tau = {}_x\tau_p^0 + {}_x\tau_\nu^0 = {}_x\tau_a^h + {}_x\tau_p^h + {}_x\tau_\nu^h. \qquad \text{(A 19)}$$

The different stresses are simplified as

$$
\begin{aligned}
{}_x\tau_\nu^h &= \mu\,\frac{\partial\overline{u}}{\partial\xi}\Big|_h + \mu\,\overline{\left(\frac{\partial\eta}{\partial x}\right)^2\frac{\partial\tilde{u}}{\partial\xi}}\Big|_h + \mu\,\overline{\left(\frac{\partial\eta}{\partial x}\right)^2}\frac{\partial\overline{u}}{\partial\xi}\Big|_h \\
&\quad - 2\mu\,\overline{\frac{\partial\eta}{\partial x}\frac{\partial\tilde{u}}{\partial x}}\Big|_h - \mu\overline{\frac{\partial^2\eta}{\partial x^2}\tilde{u}_h} - \mu\overline{\frac{\partial^2\eta}{\partial x^2}u_h''} - \mu\overline{\frac{\partial^2\eta}{\partial x^2}}\overline{u}_h \qquad \text{(A 20}a\text{)} \\
{}_x\tau_a^h &= -\rho\,\overline{\tilde{u}\tilde{w}}\Big|_h - \rho\,\overline{u''w''}\big|_h + \rho\overline{\tilde{u}_h\frac{\partial\eta}{\partial t}} + \rho\overline{\tilde{u}_h^2\frac{\partial\eta}{\partial x}} + \rho\overline{u_h''^2\frac{\partial\eta}{\partial x}} + 2\rho\overline{u}_h\overline{\tilde{u}_h\frac{\partial\eta}{\partial x}} \qquad \text{(A 20}b\text{)} \\
{}_x\tau_p^h &= \overline{\tilde{p}_h\frac{\partial\eta}{\partial x}} \qquad \text{(A 20}c\text{)} \\
{}_x\tau_\nu^0 &= \mu\,\frac{\partial\overline{u}}{\partial\xi}\Big|_0 + \mu\,\overline{\left(\frac{\partial\eta}{\partial x}\right)^2\frac{\partial\tilde{u}}{\partial\xi}}\Big|_0 + \mu\,\overline{\left(\frac{\partial\eta}{\partial x}\right)^2}\frac{\partial\overline{u}}{\partial\xi}\Big|_0 \\
&\quad - 2\mu\,\overline{\frac{\partial\eta}{\partial x}\frac{\partial\tilde{u}}{\partial x}}\Big|_0 - \mu\overline{\frac{\partial^2\eta}{\partial x^2}\tilde{u}_0} - \mu\overline{\frac{\partial^2\eta}{\partial x^2}u_0''} - \mu\overline{\frac{\partial^2\eta}{\partial x^2}}\overline{u}_0 \qquad \text{(A 20}d\text{)}
\end{aligned}
$$

$$ {}_x\tau_p^0 = \overline{\tilde{p}_0 \frac{\partial \eta}{\partial x}}. \tag{A 20e} $$

Under these conditions, equation (A 19) links stresses expressed at the surface and stresses expressed at the altitude $\xi = h$:

$$ {}_x\tau^h = {}_x\tau_a^h + {}_x\tau_p^h + {}_x\tau_v^h = {}_x\tau_p^0 + {}_x\tau_v^0 = \tau \tag{A 21} $$

where τ is total stress from wind towards waves. Thus, the pressure–slope term ${}_x\tau_p^h$ expressed at $\xi = h$ can be expressed as follows:

$$ {}_x\tau_p^h = \tau - {}_x\tau_a^h - {}_x\tau_v^h \tag{A 22} $$

where the RHS terms of equation (A 22) only depend on the velocity components.

REFERENCES

ARDHUIN, F., CHAPRON, B. & COLLARD, F. 2009 Observation of swell dissipation across ocean. *Geophys. Res. Lett.* **36**, L06607.

ARDHUIN, F. & JENKINS, A. D. 2006 On the interaction of surface waves and upper ocean turbulence. *J. Phys. Oceanogr.* **36**, 551–557.

BANNER, M. L. 1990 The influence of wave breaking on the surface pressure distribution in wind–wave interactions. *J. Fluid Mech.* **211**, 463–495.

BANNER, M. L. & MELVILLE, W. K. 1976 On the separation of air flow above water waves. *J. Fluid Mech.* **77**, 825–842.

BANNER, M. L. & PEIRSON, W. L. 1998 Tangential stress beneath wind-driven air–water interfaces. *J. Fluid Mech.* **364**, 115–145.

BANNER, M. L. & PEIRSON, W. L. 2007 Wave breaking onset and strength for two-dimensional deep-water wave groups. *J. Fluid Mech.* **585**, 93–115.

BANNER, M. L. & PHILLIPS, O. M. 1974 On the incipient breaking of small scale waves. *J. Fluid Mech.* **65**, 647–656.

BELCHER, S. E., HARRIS, J. A. & STREET, R. L. 1994 Linear dynamics of wind waves in coupled turbulent air–water flow, part 1: theory. *J. Fluid Mech.* **271**, 119–151.

BENJAMIN, T. B. & FEIR, J. E. 1967 The disintegration of wave trains on deep water. Part 1. Theory. *J. Fluid Mech.* **27**, 417–430.

BOLE, J. B. & HSU, E. Y. 1969 Response of gravity water waves to wind excitation. *J. Fluid Mech.* **35**, 657–675.

CHEUNG, T. K. & STREET, R. L. 1988 The turbulent layer in the water at an air–water interface. *J. Fluid Mech.* **194**, 133–151.

COANTIC, M., RAMAMONJIARISOA, A., MESTAYER, P., RESCH, F. & FAVRE, A. 1981 Wind water tunnel simulation of small scale ocean atmosphere interactions. *J. Geophys. Res.* **C7**, 6607–6626.

CRAIG, P. D. & BANNER, M. L. 1994 Modelling wave-enhanced turbulence in the ocean surface layer. *J. Phys. Oceanogr.* **24**, 2546–2559.

DEARDORFF, J. W. 1967 Aerodynamic theory of growth with constant wave steepness. *J. Oceanogr. Soc. Japan* **23** (6), 278–297.

DONELAN, M. A. 1990 Air-sea interaction. In *The Sea* (ed. B. Le Méhauté & D. Hanes). vol. 9A. pp. 239–292. Wiley.

DONELAN, M. A. 1999 Wind-induced growth and attenuation of laboratory waves. In *Wind-over-Wave Couplings: Perspectives and Prospects* (ed. S. G. Sajjadi, N. H. Thomas & J. C. R. Hunt). pp. 183–194. Clarendon.

DONELAN, M. A., BABANIN, A. V., YOUNG, I. R. & BANNER, M. L. 2006 Wave-follower field measurements of the wind-input spectral function. Part II: parameterisation of wind input. *J. Phys. Oceanogr.* **36**, 1672–1689.

DONELAN, M. A., BABANIN, A. V., YOUNG, I. R., BANNER, M. L. & MCCORMICK, C. 2005 Wave-follower field measurements of the wind-input spectral function. Part I: measurements and calibrations. *J. Atmos. Ocean. Technol.* **22**, 799–813.

DONELAN, M. A. & PIERSON, W. J. 1987 Radar scattering and equilibrium ranges in wind-generated waves with application to scatterometry. *J. Geophys. Res.* **92** (C5), 4971–5029.

DRAZEN, D. A. & MELVILLE, W. K. 2009 Turbulence and mixing in unsteady breaking surface waves. *J. Fluid Mech.* **628**, 85–119.

DRAZEN, D. A., MELVILLE, W. K. & LENAIN, L. 2008 Inertial scaling of dissipation in unsteady breaking waves. *J. Fluid Mech.* **611**, 307–332.

DUNCAN, J. H. 1981 An experimental investigation of breaking waves produced by a towed hydrofoil. *Proc. R. Soc. Lond.* A **377**, 331–348.

DUNCAN, J. H. 1983 The breaking and non-breaking resistance of a two-dimensional hydrofoil. *J. Fluid Mech.* **126**, 507–520.

ELLIOTT, J. A. 1970 Microscale pressure fluctuations measured within the lower atmospheric boundary layer. PhD thesis, University of Britain Columbia.

ELLIOTT, J. A. 1972*a* Microscale pressure fluctuations measured within the lower atmospheric boundary layer. *J. Fluid Mech.* **53**, 351–384.

ELLIOTT, J. A. 1972*b* Microscale pressure fluctuations near waves being generated by the wind. *J. Fluid Mech.* **54**, 427–448.

GRARE, L. 2009 Etude des interactions Océan-Atmosphère à proximité immediate de l'interface: Application aux vagues de vent et aux vagues extrêmes. PhD thesis, University of Aix-Marseille, http://tel.archives-ouvertes.fr/docs/00/45/45/11/PDF/These_Grare_070509.pdf.

JANSSEN, P. 2004 *The Interaction of Ocean Waves and Wind*. Cambridge University Press.

JEFFREYS, H. 1925 On the formation of water waves by wind. *Proc. R. Soc. Lond. Ser.* A **107** (742), 189–206.

JESSUP, A. T. & PHADNIS, K. R. 2005 Measurement of the geometric and kinematic properties of microscale breaking waves from infrared imagery using a PIV algorithm. *Meas. Sci. Technol.* **16**, 1961–1969.

JONES, I. S. F. & TOBA, Y. 2001 *Wind Stress Over the Ocean*. Cambridge University Press.

KAWAMURA, H., OKUDA, K., KAWAI, S. & TOBA, Y. 1981 Structure of turbulent boundary layer over wind waves in a wind tunnel. *Tohoku Geophys. J.* **28**, 69–86.

KOMEN, G. J., CAVALERI, M., DONELAN, M., HASSELMANN, K., HASSELMANN, S. & JANSSEN, P. A. E. M. 1994 *Dynamics and Modelling of Ocean Waves*. Cambridge University Press.

LATIF, M. A. 1974 Acoustic effects on pressure measurements over water waves in the laboratory. *Tech. Rep.* no 25. Coastal and Oceanographic Engineering Laboratory.

LONGUET-HIGGINS, M. S. 1969 A nonlinear mechanism for the generation of sea waves. *Proc. R. Soc. Lond.* A **311**, 371–389.

LONGUET-HIGGINS, M. S. 1992 Capillary rollers and bores. *J. Fluid Mech.* **240**, 659–679.

LONGUET-HIGGINS, M. S. & STEWART, R. W. 1964 Radiation stresses in water waves: a physical discussion with applications. *Deep-Sea Res.* **11**, 529–562.

MAKIN, V. K., BRANGER, H., PEIRSON, W. L. & GIOVANANGELI, J.-P. 2007 Stress above wind-plus-paddle waves: modelling of laboratory experiment. *J. Phys. Oceanogr.* **37** (12), 2824–2837.

MASTENBROEK, C., MAKIN, V. K., GARAT, M. H. & GIOVANANGELI, J.-P. 1996 Experimental evidence of the rapid distortion of turbulence in the air flow over water waves. *J. Fluid Mech.* **318**, 273–302.

MELLOR, G. L. & BLUMBERG, A. F. 2004 Wave breaking and ocean surface layer thermal response. *J. Phys. Oceanogr.* **34**, 693–698.

MELVILLE, W. K. & MATUSOV, P. 2002 Distribution of breaking waves at the ocean surface. *Nature* **417**, 58.

MELVILLE, W. K., VERON, F. & WHITE, J. W. 2002 The velocity field under breaking waves: coherent structures and turbulence. *J. Fluid Mech.* **454**, 203–233.

MILES, J. W. 1957 On the generation of surface waves by shear flows. *J. Fluid Mech.* **3**, 185–204.

MILES, J. W. 1959 On the generation of surface waves by shear flows. Part 2. *J. Fluid Mech.* **6**, 568–582.

MITSUYASU, H. & HONDA, T. 1982 Wind-induced growth of water waves. *J. Fluid Mech.* **123**, 425–442.

PAPADIMITRAKIS, Y., HSU, E. & STREET, R. 1984 Measurements of the fluctuating pressure in the turbulent boundary layer over progressive mechanically generated water waves. In *Gas Transfer at Water Surfaces* (ed. W. Brutsaert & G. H. Jirka). Kluwer.

PEIRSON, W. L. 1997 Measurement of surface velocities and shears at a wavy air–water interface using particle image velocimetry. *Exp. Fluids* **23**, 427–437.

PEIRSON, W. L. & BANNER, M. L. 2001 On the strength of breaking of deep water waves. In *Proc. Int. Conf. Coastal Engineering*. ASCE.

PEIRSON, W. L. & BANNER, M. L. 2003 Aqueous surface layer flows induced by microscale breaking wind waves. *J. Fluid Mech.* **479**, 1–38.

PEIRSON, W. L. & BELCHER, S. E. 2005 Growth Response of Waves to the Wind Stress. In *Proc. Int. Conf. Coastal Engineering*. ASCE.

PEIRSON, W. L., BEYA, J. F., BANNER, M. L., PERAL, J. S. & AZARMA, S. A. 2013 Rain-induced attenuation of water waves. *J. Fluid Mech.* Accepted for publication 26 January 2013.

PEIRSON, W. L. & GARCIA, A. W. 2008 On the wind-induced growth of slow water waves of finite steepness. *J. Fluid Mech.* **608**, 243–274.

PEIRSON, W. L., GARCIA, A. W. & PELLS, S. E. 2003 Water–wave attenuation due to opposing wind. *J. Fluid Mech.* **487**, 345–365.

PEIRSON, W. L., WALKER, J. W. & BANNER, M. L. 2012 On the microphysical behaviour of wind-forced water surfaces and consequent re-aeration. *J. Fluid Mech.* (submitted).

PHILLIPS, O. M. 1977 *The Dynamics of the Upper Ocean*. Cambridge University Press.

PHILLIPS, O. M. 1985 Spectral and statistical properties of the equilibrium range in the wind-generated gravity waves. *J. Fluid Mech.* **156**, 505–531.

PLANT, W. J. 1982 A relationship between wind stress and wave slope. *J. Geophys. Res.* **87** (C3), 1961–1967.

PLANT, W. J., DHAL, P. H. DAHL, GIOVANANGELI, J.-P. & BRANGER, H. 2004 Bound and free surface waves in a large wind–wave tank. *J. Geophys. Res. C: Oceans* **109**, C10002.

RAMAMONJIARISOA, A. & COANTIC, M. 1976 Loi expérimentale de dispersion des vagues produites par le vent sur une faible longueur d'action. *C. R. Acad. Sci.* **282**, 111–114.

RAPP, R. J. & MELVILLE, W. K. 1990 Laboratory measurements of deep water breaking waves. *Phil. Trans. R. Soc. Lond.* A **331**, 735–800.

REUL, N., BRANGER, H., BLIVEN, L. & GIOVANANGELI, J. P. 1999 The influence of oblique waves on the azimuthal response of a Ku-band scatterometer. *IEEE Trans. Geosci. Remote Sens.* **37** (1), 36–47.

REUL, N., BRANGER, H. & GIOVANANGELI, J.-P. 2008 Air flow structure over short-gravity breaking water waves. *Boundary-Layer Meteorol.* **126**, 477–505.

ROMERO, L., MELVILLE, K. M. & KLEISS, J. 2012 Spectral energy dissipation due to surface–wave breaking. *J. Phys. Oceanogr.* **42**, 1421–1444.

SHEMDIN, O. H. & HSU, E. Y. 1967 Direct measurements of aerodynamic pressure above a simple progressive gravity wave. *J. Fluid Mech.* **30**, 403–416.

SNYDER, R. L., DOBSON, F. W., ELLIOTT, J. A. & LONG, R. B. 1981 Array measurements of atmospheric pressure fluctuations above surface gravity waves. *J. Fluid Mech.* **102**, 1–59.

SULLIVAN, P. P. & MCWILLIAMS, J. C. 2010 Dynamics of winds and currents coupled to surface waves. *Annu. Rev. Fluid Mech.* **42**, 19–42.

TEIXEIRA, M. A. & BELCHER, S. E. 2002 On the distortion of turbulence by a progressive surface wave. *J. Fluid Mech.* **458**, 229–267.

THAIS, L. & MAGNAUDET, J. 1996 Turbulent structure beneath surface gravity waves sheared by the wind. *J. Fluid Mech.* **328**, 313–344.

TIAN, Z., PERLIN, M. & CHOI, W. 2010 Energy dissipation in two-dimensional unsteady plunging breakers and an eddy viscosity model. *J. Fluid Mech.* **655**, 217–257.

TOLMAN, H. 2009 User manual and system documentation of WAVEWATCH III^{TM}version 3.14. Technical note. MMAB Contribution No. 276. NOAA.

VERON, F., SAXENA, G. & MISRA, S. K. 2007 Measurements of the viscous tangential stress in the airflow above wind waves. *Geophys. Res. Lett.* **34**, L19603.

WALKER, J. W. 2009 The exchange of oxygen at the surface of open waters under wind forcing. PhD thesis, School of Civil and Environmental Engineering. The University of New South Wales. http://unsworks.unsw.edu.au/fapi/datastream/unsworks:5256/SOURCE02.

WANNINKHOF, R., ASHER, W. E., HO, D. T., SWEENEY, C. S. & MCGILLIS, W. R. 2009 Advances in quantifying air–sea gas exchange and environmental forcing. *Annu. Rev. Mar. Sci.* **1**, 213–244.

WILSON, W. S., BANNER, M. L., FLOWER, R. J., MICHAEL, J. A. & WILSON, D. G. 1973 Wind-induced growth of mechanically generated water waves. *J. Fluid Mech.* **58**, 435–460.

WU, J. 1975 Wind-induced drift currents. *J. Fluid Mech.* **68**, 49–70.

WU, H.-Y., HSU, E.-Y. & STREET, R. L. 1977 The energy transfer due to air-input, nonlinear wave–wave interactions and white-cap dissipation associated with wind-generated waves. *Dept. Civ. Eng. Tech Rep.* No. 207, Stanford University, Stanford, California.

WU, H.-Y., HSU, E.-Y. & STREET, R. L. 1979 Experimental study of non-linear wave–wave interaction and white-cap dissipation of wind-generated waves. *Dyn. Atmos. Oceans* **3**, 55–78.

ZHANG, X. 2002 Enhanced dissipation of short gravity and gravity capillary waves due to parasitic capillaries. *Phys. Fluids* **14** (742), 81–84.